Chemical Engineering Science 270 (2023) 118511

Contents lists available at ScienceDirect

Chemical Engineering Science

journal homepage: www.elsevier.com/locate/ces

# On the effect of turbulent fluctuations on precipitation: A direct numerical simulation – population balance study

Hin Yan Tang [a], Stelios Rigopoulos [a,*], George Papadakis [b]

[a] Department of Mechanical Engineering, Imperial College London, South Kensington Campus, London SW7 2AZ, UK
[b] Department of Aeronautics, Imperial College London, Exhibition Road, SW7 2AZ London, UK

## HIGHLIGHTS

- Precipitation of $BaSO_4$ in a T-mixer is investigated via DNS and discretised PBE.
- Unclosed terms in the population balance in turbulent flow are computed by DNS.
- Fluctuations found to have important implications for modelling.
- Higher Sc results in thinner reaction zones with higher reaction rates.
- Effect of higher Sc on the PSD is marginal due to competing effects of the above.

## ARTICLE INFO

*Article history:*
Received 6 September 2022
Received in revised form 13 January 2023
Accepted 20 January 2023
Available online 25 January 2023

*Keywords:*
Precipitation
Turbulence
Mixing
Population balance
DNS
High Schmidt number

## ABSTRACT

The objective of the present paper is to investigate the effect of turbulent fluctuations on precipitation and the implications for modelling. To this end, a coupled direct numerical simulation (DNS) - population balance study is conducted on the experiments of Schwarzer et al. (2006) on $BaSO_4$ precipitation in a T-mixer. The unclosed terms in the averaged population balance equation are identified and evaluated via DNS. A comparison of the average nucleation and growth rates with those computed with the average values shows significant deviations indicative of the importance of fluctuations in precipitation modelling. Furthermore, the correlation between growth and number density is analysed, as well as its contribution to the reactant consumption. The study is performed at $Sc = 1$ as it is, at present, not possible to resolve the sub-Kolmogorov scales at high Reynolds and Schmidt numbers. However, an attempt to investigate the effect of sub-Kolmogorov scales is made by performing a simulation of precipitation in a similar T-mixer at a lower (but still turbulent) Reynolds number and at $Sc = 1$ and $Sc = 10$. The findings indicate the presence of thinner reaction zones at higher $Sc$, but the effect on the product particle size distribution is marginal. An analysis of the results indicates that this is due to a compensation of the effect of thinner reaction zones by higher reaction rates occurring therein.



## 1. Introduction

Reaction crystallisation, or precipitation, is a process for synthesising particulate products in aqueous solutions and has numerous applications, including the formation of active pharmaceutical ingredients and production of nanoparticles. The formation of particles is a thermodynamic and kinetic process that involves nucleation, growth and possibly aggregation and breakage. The resultant particles are polydispersed in size and the particle size distribution (PSD) has direct impact on the product quality and suitability for specific applications. Predictive simulations are therefore required for process design, optimisation and scale-up to produce tailor-made products.

The evolution of the PSD is governed by the population balance equation (PBE), which describes the dynamics of the particle population as a result of the underlying transport and kinetic processes. In a precipitation process that invovles mixing and fast reactions, strong spatial variations of reactant species result in a spatially dependent PSD, suggesting that the PBE should be coupled with fluid dynamics. Since most mixers involve turbulent flow, this coupling involves complex issues regarding both model formulation and solution method (Bałdyga and Bourne, 1999; Rigopoulos, 2010; Marchisio and Fox, 2013). In particular, the fluctuations in concentrations of reacting species result in fluctuating nucleation and growth rates. In the case of fast reactions, such

* Corresponding author.
*E-mail address:* s.rigopoulos@imperial.ac.uk (S. Rigopoulos).

https://doi.org/10.1016/j.ces.2023.118511
0009-2509/

fluctuations occur within small space and time scales that may not be resolved even by Large Eddy Simulation (LES). Mathematically, these fluctuations manifest themselves in the form of unclosed terms in the averaged or filtered PBE (Rigopoulos, 2007). A similar closure problem occurs in turbulent combustion, where concentration and temperature fluctuations in conjunction with non-linear kinetics lead to an unclosed reaction source term, and inaccurate modelling of the latter can result in incorrect prediction of features such as ignition, extinction and pollutant formation. While the turbulent combustion closure problem has been studied with a number of methods (Peters, 2000; Poinsot and Veynante, 2005), studies on the impact of fluctuations on turbulent precipitation and its modelling have been far more limited.

The modelling studies of turbulent precipitation can be distinguished in terms of the approach they take to the coupling of population balance, chemistry and flow, as well as in terms of the method employed for the numerical solution of the PBE. With respect to the former, we must distinguish between lumped models that approximate the mixing device as an ideal reactor or a network of ideal reactors and models based on computational fluid dynamics (CFD). With respect to the solution method, approaches are either based on the method of moments, which solves for integral properties of the PSD (such as total number or total volume of particles), or on a discretised population balance (also known as sectional method), which solves for the complete PSD.

Lumped models greatly reduce the number of population balance equations to be solved but incur a major simplification of the effect of fluid dynamics. Mixing effects may be taken into account via parametrisation of the reactor network with quantities such as the turbulent kinetic energy and its dissipation rate. A review of early works in this category can be found in Tavare (1986). Pohorecki and Bałdyga (1983, 1988) employed ideal reactor models together with a phenomenological micromixing model to describe precipitation in stirred tank reactors, while a more comprehensive analysis of this problem was presented by Bałdyga et al. (1995) based on the Engulfment and the Engulfment-Deformation-Diffusion (EDD) models (Bałdyga and Bourne, 1984; Bałdyga and Bourne, 1984; Bałdyga and Bourne, 1999). The effect of micromixing on precipitation was also explored in the works by Marcant and David (1991, 1994), while some general rules were extracted by David (2001), with the acknowledgement that they only represent broad trends. Lumped models can be complemented by CFD simulations, which can provide parameters such as energy dissipation rate, while being, however, decoupled from the precipitation model. This approach has been adopted, for example, by Zauner and Jones (2000), who employed Villermaux's Segregated Feed Model (SFM) (Villermaux, 1989), and by Schwarzer and Peukert (2004a,b), who employed a modified version of the EDD model. A general methodology for coupling compartmental models with CFD was proposed by Rigopoulos and Jones (2003). However, precipitation mechanisms often have very short time scales and take place within very thin zones, resulting in strong spatial gradients whose effect cannot be captured with a lumped approach. The use of a micromixing model in the context of a compartmental model does allow for incorporating mixing effects to a certain extent, but overall the lumped approach relies on phenomenological models and empirical parameters.

The first studies of turbulent precipitation with CFD (Seckler et al., 1995; Van Leeuwen et al., 1996; Wei and Garside, 1997; Wei et al., 2001; Jaworski and Nienow, 2003; Öncül et al., 2006) were based on the Reynolds-Averaged Navier–Stokes (RANS) equations. While this approach provides the mean flow field, reactant and particle distribution (albeit subject to the assumptions and limitations of the turbulence model employed), the scales at which precipitation occurs are not unresolved. The mixing at the small scales, or micromixing, was ignored in these studies, but its importance was acknowledged or debated; for example, Van Leeuwen et al. (1996) ascribed to it the faster reaction progress in the simulation as compared with the experiment (which employed jet mixing), while Jaworski and Nienow (2003) argued that it would be less important in the stirred tank experiments they conducted.

Bałdyga and Orciuch (1997, 2001, 2003, 2007) proposed a micromixing closure for RANS based on a presumed $\beta$-PDF model. The mixing process was described in terms of a mixture fraction (the volume fraction originating in one of the inlets). By assuming that the mixture fraction has a $\beta$-PDF, it was possible to obtain closure of the non-linear terms in the population balance while accounting for fluctuations. This approach was also adopted by Vicum and Mazzotti (2007). Piton et al. (2000) and Marchisio et al. (2001) employed a presumed finite-mode PDF model where the PDF of mixture fraction is given as a sum of delta functions. Later works based on the presumed PDF approach include Gavi et al. (2007). In all of these works, the method of moments was employed for the solution of the population balance.

While presumed PDF methods represent one way of accounting for micromixing, they still involve assumptions on PDF shape. Transported PDF closures, on the other hand, overcome this issue but typically require stochastic methods for numerical solution, and furthermore certain unclosed terms related to turbulent transport and diffusion remain. Transported PDF closures have been explored in combustion (Haworth, 2010) where they have proven to be very beneficial for overcoming the issue of turbulence-chemistry interaction and closing the highly non-linear source terms. They have also been applied to precipitation in conjunction with the method of moments (Marchisio et al., 2001) and by Falk and Schaer (2001), and with discretised population balance by Woo et al. (2006) and Di Veroli and Rigopoulos (2009, 2010).

More advanced simulations, in terms of fluid dynamics, have appeared in recent years. Makowski et al. (2012) employed LES while neglecting subgrid fluctuations and compared with a RANS approach that accounted for them with the presumed PDF method proposed in the earlier work of Bałdyga and Orciuch (1997, 2001). The LES was shown to provide better results at low Reynolds numbers and furthermore the difference between the two models increased with supersaturation. Metzger and Kind (2015, 2017) employed a transient detached eddy simulation for a confined impinging jet mixer.

In recent years, Direct Numerical Simulation (DNS) has arisen as a tool for investigating fundamental questions to aid the development of improved models. Schwarzer et al. (2006) (see also Gradl et al., 2006, 2009), presented a DNS-PBE study where the PBE was solved along a number of Lagrangian trajectories at a post-processing level. A fully coupled DNS-PBE methodology was later presented by Tang et al. (2020), featuring a discretised PBE solved in the whole domain. Recently, Tang et al. (2022) conducted a study of precipitation in a T-mixer that coupled DNS with PBE with the aim of investigating the interaction of turbulence with nucleation and growth. Based on the experiments of Schwarzer et al. (2006) on $BaSO_4$ precipitation in a T-mixer, their work showed that the fluctuations in reactant concentrations give rise to highly intermittent precipitation rates, particularly in nucleation which features strongly non-linear kinetics. Thin nucleation zones were identified, corresponding to nucleation bursts. Furthermore, the turbulence and kinetic time scales were found to be comparable throughout the domain, indicating that the process is neither mixing nor kinetics controlled. At a Reynolds number of 1135, it was not possible to resolve the scales below the Kolmogorov scale (i.e. down to the Batchelor scale) that appear in high Schmidt number flows.

While the aforementioned studies elucidated the role of turbulent mixing in precipitation, further questions remain regarding

the implications on modelling and applications. As shown by the preceding literature survey, some approaches opt for neglecting the effect of turbulent fluctuations on the population balance. On the other hand, models such as the $\beta$-PDF impose assumptions on the probability density functions of scalars arising from the mixing process, while the transported PDF approach is more comprehensive but also more computationally expensive and still not free of modelling assumptions. DNS could shed light on these questions by evaluating the unclosed terms that result from the averaging of the PBE in turbulent flow.

The role of high Schmidt number in liquid mixing is another unknown in precipitation modelling. At high Schmidt number, scales smaller than the Kolmogorov scale, $\eta$, appear in scalar transport. These scales go down to the Batchelor scale, $\eta_c$, which is related to the former as $\eta_c = \eta/\sqrt{Sc}$ (Davidson, 2004). The resolution of $\eta_c$ in practical problems and for $Sc$ in the order of 1000 (as is common in precipitation) is out of reach of computational capability at present or in the foreseeable future. Although investigations on high Schmidt number transport have appeared recently in the literature (Donzis et al., 2010; Donzis and Yeung, 2010; Derksen, 2012; Donzis et al., 2014; Buaria et al., 2021; Ranjan and Menon, 2021), the focus of these studies has been mainly on passive and inert scalars, and most of them have been conducted in isotropic turbulence. As such, the understanding of the effect of Schmidt number on reacting flows in the liquid phase is still limited. A recent work by Leer et al. (2022) promises a way forward by proposing a hybrid Eulerian–Lagrangian approach.

The present study aims to address these gaps. First, an evaluation of the unclosed terms in the averaged PBE is performed via the DNS-PBE methodology introduced by Tang et al. (2020), where the PBE is discretised and the flow is resolved down to the Kolmogorov scale. Each unclosed term is studied on its own and appropriate comparisons are made to assess its magnitude and importance. The case under investigation is the precipitation of $BaSO_4$ in a T-mixer reported in the experiments of Schwarzer et al. (2006). Second, although it is not possible, at present, to resolve the sub-Kolmogorov scales at the Reynolds and Schmidt numbers of the aforementioned study, we carry out a preliminary assessment of their effect on precipitation. To this end, a configuration is set up with a geometry similar to the one studied by Tang et al. (2022) and with $Re = 400$ and $Sc = 10$, which are the lowest values that permit resolution of the Batchelor scale with the available resources while still ensuring a turbulent - just over the transition $Re$ for T-mixers (Telib et al., 2004) - flow. By comparing with a simulation in the same configuration at $Sc = 1$, it is possible to examine the effect of the sub-Kolmogorov scales on the reaction zones and their ultimate effect on the precipitation outcome.

The structure of the paper is as follows. In Section 2, the unclosed terms in the averaged PBE are identified and a strategy for their evaluation is proposed. Section 3 describes the general aspects of the methodology employed in the present study, including the discretisation of the PBE and the precipitation kinetics. Section 4 contains the analysis of the unclosed terms for the $Re = 1135$ and $Sc = 1$ case where the Kolmogorov scale is resolved. The sub-Kolmogorov scales on the $Re = 400$ and $Sc = 10$ case are investigated in Section 5, followed by a summary of the main findings.

## 2. The closure problem for population balance in turbulent flow

### 2.1. Governing equations

In a problem featuring strong spatial variations of particle concentration, the local PSD can be represented by a number density concentration field, $n(v, \mathbf{x}, t)$, such that $n(v, \mathbf{x}, t)dv$ represents the concentration of particles whose volume falls between $v$ and $v + dv$ at location $\mathbf{x}$ and time $t$. For a process involving nucleation and growth of particles, the evolution of the local PSD is described by the following spatially-dependent PBE:

$$\frac{\partial n}{\partial t} + \frac{\partial (u_i n)}{\partial x_i} + \frac{\partial (Gn)}{\partial v} = D_p \frac{\partial^2 n}{\partial x_i \partial x_i} + B\delta(v - v_0) \tag{1}$$

where $u_i$ is the fluid velocity, $D_p$ is the particle diffusivity, $B$ is the nucleation rate and $G$ is the growth rate. A few notes should be made about the assumptions inherent in Eq. 1. In the case under consideration in the present paper, aggregation is suppressed due to electrostatic repulsion (Schwarzer and Peukert, 2005; Kucher et al., 2006), and is thus not included in Eq. 1. Furthermore, a particle acceleration term is not included because, for the nanoparticles considered in the present study, the Stokes number (equal to the ratio of the particle relaxation time to a characteristic flow timescale) is close to zero and the particles thus follow the fluid motion. The flow to be considered is isothermal and therefore the diffusivity is not spatially varying. Finally, it should be mentioned that the PBE may also be formulated in terms of particle diameter; in the present paper, a volume-based formulation is used for consistency with our previous works that developed or used the numerical method employed here for the solution of the PBE (Liu and Rigopoulos, 2019; Liu et al., 2020; Tang et al., 2020; Tsagkaridis et al., 2022; Sun and Rigopoulos, 2022). It must be emphasised that the method has been developed for population balance problems that may include aggregation and fragmentation (O'Sullivan and Rigopoulos, 2022), for which a volume-based formulation is advantageous, and these processes may also be affected by turbulent fluctuations (see Tsagkaridis et al. (2022) for a study of the effect of turbulent fluctuations on a population balance problem with aggregation).

The nucleation and growth rates are functions of local composition, and therefore a transport equation for the concentration of each chemical species, $C_\alpha$, must be solved together with the PBE. This equation is shown below, also for isothermal flow (hence constant diffusivity):

$$\frac{\partial C_\alpha}{\partial t} + \frac{\partial (u_i C_\alpha)}{\partial x_i} = D_\alpha \frac{\partial^2 C_\alpha}{\partial x_i \partial x_i} + R_\alpha \tag{2}$$

where $R_\alpha$ is the reaction source term that involves, apart from chemical reactions, the nucleation and growth kinetics, thus providing the coupling with the PBE. It is instructive to write its form for a precipitation process described by an instantaneous reaction (as is often the case with ionic reactions) between two species, $A$ and $B$, forming a crystal, $C_s$:

$$\nu_\alpha A + \nu_\beta B \rightarrow C_s$$

In this case, the reaction source term can be written in terms of the volumetric formation rate of crystals as follows:

$$R_\alpha = \frac{\nu_\alpha \rho_c}{MW_c}\left[B v_0 - \int v \frac{\partial (Gn)}{\partial v} dv\right] \tag{3}$$

where $\rho_c$ is the density of the crystals and $MW_c$ is their molecular weight. Note that, in this case, the reaction rate is given solely by the nucleation and growth rate, due to the reaction being instantaneous; if intermediate reaction steps with finite rate kinetics were involved, they would also have been included in the reaction source term.

Finally, the PBE and species transport equations must be coupled with the continuity and Navier–Stokes equations:

$$\frac{\partial u_i}{\partial x_i} = 0 \tag{4}$$

$$\frac{\partial u_i}{\partial t} + u_j \frac{\partial u_i}{\partial x_j} = -\frac{1}{\rho}\frac{\partial p}{\partial x_i} + \nu \frac{\partial^2 u_i}{\partial x_j \partial x_j} \tag{5}$$

where we have assumed incompressible flow, constant kinematic viscosity and no body forces.

### 2.2. Averaging of the PBE and the closure problem

In a turbulent flow, every variable is subject to fluctuations. Apart from the velocity and composition, this applies also to the number density concentration and the nucleation and growth rates:

$$u_i = \langle u_i \rangle + u' \tag{6a}$$
$$C_\alpha = \langle C_\alpha \rangle + C'_\alpha \tag{6b}$$
$$n = \langle n \rangle + n' \tag{6c}$$
$$B = \langle B \rangle + B' \tag{6d}$$
$$G = \langle G \rangle + G' \tag{6e}$$

Note that $\langle B \rangle$ and $\langle G \rangle$ are *not* closed terms. This is because the averaged equations are derived for $\langle u_i \rangle, \langle C_\alpha \rangle$ and $\langle n \rangle$ only. The reason why $B$ and $G$ are fluctuating is their dependence on the concentrations of reacting species, which will be shown in Section 3.2 for the case of $BaSO_4$. In general, precipitation kinetics are non-linear, and therefore:

$$\langle B(C_1, \ldots, C_m) \rangle \neq B(\langle C_1 \rangle, \ldots, \langle C_m \rangle) \tag{7a}$$
$$\langle G(C_1, \ldots, C_m) \rangle \neq G(\langle C_1 \rangle, \ldots, \langle C_m \rangle) \tag{7b}$$

where $m$ is the number of species. The investigation of these two inequalities is one of the main objectives of the present paper.

The fluctuations in the number density concentration are due to turbulent transport and fluctuations in concentrations of reacting species, which subsequently induce fluctuations in the nucleation and growth rates. The averaging of the PBE yields:

$$\frac{\partial \langle n \rangle}{\partial t} + \frac{\partial (\langle u_i \rangle \langle n \rangle)}{\partial x_i} + \frac{\partial \langle u'_i n' \rangle}{\partial x_i} + \frac{\partial (\langle G \rangle \langle n \rangle)}{\partial v} + \frac{\partial \langle G' n' \rangle}{\partial v} = D_p \frac{\partial^2 \langle n \rangle}{\partial x_i \partial x_i} + \langle B \rangle \delta(v - v_0) \tag{8}$$

where the terms involving $\langle u'_i n' \rangle, \langle G' n' \rangle, \langle B \rangle$ and $\langle G \rangle$ are unclosed. The first of these quantities represents turbulent transport of particles and, for non-inertial particles, behaves in a similar way as the turbulent transport of a scalar. The other three terms are unique to population balance problems and their study is the objective of the present paper.

The averaged PBE must be coupled with the equations for the average velocity and reactive species. The species transport equation deserves further attention, as it is coupled with the PBE via the consumption of species due to nucleation and growth. The averaging of the scalar transport equation yields:

$$\frac{\partial \langle C_\alpha \rangle}{\partial t} + \frac{\partial (\langle u_i \rangle \langle C_\alpha \rangle)}{\partial x_i} + \frac{\partial \langle u'_i C'_\alpha \rangle}{\partial x_i} = D_\alpha \frac{\partial^2 \langle C_\alpha \rangle}{\partial x_i \partial x_i} + \langle R_\alpha \rangle \tag{9}$$

where the unclosed term $\langle u'_i C'_\alpha \rangle$ represents turbulent transport of species $\alpha$, while the average of the source term is unclosed due to the non-linearity of the latter. For the case of an instantaneous reaction where the source term is given by Eq. 3, the averaged source term is given by:

$$\langle R_\alpha \rangle = \frac{\nu_\alpha \rho_c}{MW_c} \left[ \langle B \rangle v_0 - \int v \left[ \frac{\partial (\langle G \rangle \langle n \rangle)}{\partial v} + \frac{\partial \langle G' n' \rangle}{\partial v} \right] dv \right] \tag{10}$$

It can be seen that the non-linear unclosed terms $\langle B \rangle$ and $\langle G' n' \rangle$ also appear here and thus render the average reaction term unclosed. A more complex reaction system that includes intermediate steps with finite rate kinetics would involve further non-linearities.

In the present work, the equations to be solved are not the averaged equations shown above but rather Eqs. 4, 5, 1, and 2 that describe the instantaneous fields of velocity, concentration and number density, via the DNS-PBE methodology to be described in the following section. The results will then be processed to extract the following quantities:

- Difference between mean nucleation rate and nucleation rate computed with mean concentrations: $\langle B \rangle - B(\langle C_1 \rangle, \ldots, \langle C_m \rangle)$.
- Difference between mean growth rate and growth rate computed with mean concentrations: $\langle G \rangle - G(\langle C_1 \rangle, \ldots, \langle C_m \rangle)$.
- Particle number density - growth correlation: $\langle G' n' \rangle$ that appears in Eq. 8 as $\partial \langle G' n' \rangle / \partial v$ as well as in Eq. 9 as $\int (v \partial \langle G' n' \rangle / \partial v) dv$ (see also Eq. 10).

These are the quantities that encapsulate the effect of turbulent fluctuations on precipitation. It should be mentioned that similar unclosed terms occur in the filtering of the PBE for LES.

## 3. Methodology

### 3.1. DNS-PBE Modelling Approach

The approach for coupling DNS and PBE that will be used in the present paper was proposed and implemented by Tang et al. (2020). It combines a DNS that resolves the flow field and scalar transport with a discretisation (sectional) method for solving the PBE and predicting the PSD. The PBE allows the calculation of the reactant consumption during the crystallisation process, which enters the scalar transport equations as a source term, thus coupling the PBE with the DNS. It must be mentioned that the overall DNS-PBE approach is a direct numerical simulation with respect to the carrier flow only, where the Navier–Stokes equations are solved without a turbulence model, while the PBE does involve kinetic models for nucleation and growth. This is why the approach should still be validated with experimental results, and such a validation has been carried out in Tang et al. (2020).

The discretisation of the PBE results in the following set of equations for the number density in interval $k$, which contains the particles in the range between $v_{k-1}$ and $v_k$:

$$\frac{\partial n_k}{\partial t} + \frac{\partial (u_i n_k)}{\partial x_i} + \frac{\partial (G n_k)}{\partial v} = D_p \frac{\partial^2 n_k}{\partial x_i \partial x_i} + B \delta(v - v_0) \tag{11}$$

When employing a discretisation method for the PBE, care must be taken to limit numerical diffusion in the particle volume domain. In our approach, this issue is addressed via a combination of a TVD scheme (Qamar et al., 2006) and a composite grid (Tang et al., 2020). The DNS is performed with the in–house code Pantarhei, which has been used extensively to simulate transitional and turbulent flows in boundary layers, around airfoils, behind fractal grids and inside stirred vessels (Xiao and Papadakis, 2017; Xiao and Papadakis, 2019; Thomareis and Papadakis, 2017; Thomareis and Papadakis, 2018; Paul et al., 2018; Başbuğ et al., 2018). The population balance modelling is performed with the in–house code CPMOD that has been developed and tested on a variety of problems including precipitation, aerosol synthesis and soot formation (Sewerin and Rigopoulos, 2017; Sewerin and Rigopoulos, 2018; Liu and Rigopoulos, 2019; Tang et al., 2020; Sun et al., 2021). For further details on the methodology, including the spatial and temporal discretisation of the PBE, the reader may refer to Tang et al. (2020).

The particles are assumed to follow the flow, as the Stokes number is approximately zero, while a unity Schmidt number is employed for all species and particles. The latter assumption requires some further elaboration. Both species and particles have

very low diffusivities, and thus high $Sc$ numbers. This means that the transport of these quantities takes place at scales lower than the Kolmogorov scale, down to the Batchelor scale. The latter scales with the Kolmogorov scale at a rate of $1/\sqrt{Sc}$ (Davidson, 2004), which means that its resolution is not possible with current or even foreseeable computational resources (for example, for $Sc = 1000$, the Batchelor scale is $\sqrt{1000} \approx 32$ times smaller than the Kolmogorov scale; to maintain a ratio $(\Delta x/\eta_c)$ of about 2, the grid spacing $\Delta x$ should be around 30 times finer in each direction, which would mean 570 billion cells in the context of the present simulation). While there have been investigations of the effect of $Sc$ on passive scalars (Donzis et al., 2010; Donzis and Yeung, 2010; Derksen, 2012; Donzis et al., 2014; Buaria et al., 2021; Ranjan and Menon, 2021), such works have not been conducted yet for reacting flows such as the present one. The use of a high $Sc$ number without the resolution of the Batchelor scale is not an appropriate solution and would require a TVD scheme to suppress the resulting numerical oscillations, which would amount to adding artificial diffusion in a manner similar to the use of $Sc = 1$. For these reasons, a $Sc$ of one is used in Section 4 on the investigation of fluctuations down to Kolmogorov scale; as shown in our previous work (Tang et al., 2020), this assumption produced good matching with experimental results, indicating that it does not have a dominant effect. However, this assumption will be revisited in Section 5, where simulations with $Sc$ = 1 and 10 are compared in a configuration where the latter is computationally feasible.

### 3.2. Kinetics of $BaSO_4$ precipitation

The case to be considered in the present paper is the precipitation of barium sulphate from barium chloride and sulphuric acid, according to the following reaction:

$$BaCl_2 + H_2SO_4 \rightarrow BaSO_4 + 2HCl$$

The driving force for precipitation is supersaturation, which is related to the concentration of ions as follows (Vicum et al., 2003):

$$S = \gamma_{\pm}\sqrt{\frac{C_{Ba^{2+}_{(\text{free})}}\, C_{SO^{2-}_{4(\text{free})}}}{K_{SP}}} \tag{12}$$

The value of the solubility product, $K_{SP}$, is taken from Monnin (1999). Activity-based supersaturation is employed due to the high ionic strength encountered and the activity coefficient is obtained with the modified Debye-Hückel method (Bromley, 1973). Note that, because of the dissociation of $H_2SO_4$ into $H^+$ and $HSO_4^-$ (which subsequently yields $H^+$ and $SO_4^{2-}$), as well as the ion complex formation of $BaSO_4$(aq), only the free ions in the suspension are considered in the supersaturation calculation, hence the subscript 'free'. The dissociation and equilibrium constant are taken from Monnin (1999) and Schwarzer and Peukert (2004a), respectively.

Because of the high supersaturation encountered in the case under consideration, homogeneous nucleation and transport-controlled growth are the dominant mechanisms. The kinetics are taken from Mersmann (2001) and have also been employed in other works on the same case (Gradl and Peukert, 2009) and other cases with similar conditions (Gavi et al., 2007; Marchisio et al., 2006; Metzger and Kind, 2017). The equations are shown below:

$$B_N = 1.5 D_{AB}\left(\sqrt{K_{SP}} S N_A\right)^{7/3} \sqrt{\frac{\gamma_{CL}}{kT}} V_m \exp\left[-\frac{16}{3}\left(\frac{\gamma_{CL}}{kT}\right)^3 \frac{V_m^2}{(\nu \ln S)^2}\right] \tag{13}$$

$$G_L = \frac{k_a}{3k_v}\frac{Sh D_{AB}\sqrt{K_{SP}} M (S-1)}{\rho_C L} \tag{14}$$

where $B_N$ is the nucleation rate in terms of particle number (related to $B$ in Eq. 1 as $B_N = B d v_0$), while $N_A, k, D_{AB}, V_m, \gamma_{CL}, \nu$ and $\rho_C$ are the Avogadro number, Boltzmann constant, apparent diffusion coefficient, volume of $BaSO_4$ molecule, interfacial energy, dissociation number and crystal density, respectively. The values of these parameters are obtained from Refs. (Mersmann, 2001; Monnin, 1999; Schwarzer and Peukert, 2004b). The growth rate, $G_L$, described by Eq. 14 is a linear growth rate and includes the surface, $k_a$, and volume, $k_v$, shape factors for spherical particles of $\pi$ and $\pi/6$, respectively, in accordance with the experimental observations of Schwarzer et al. (2002) where oval-like and spherical shapes were observed. Eq. 1 employs the volumetric growth rate, which can be obtained as follows:

$$G = 3k_v^{1/3} \nu^{2/3} G_L \tag{15}$$

The apparent diffusion coefficient, $D_{AB}$, is computed from the diffusivities of ions, $D_A$ and $D_B$, as follows (Mersmann, 2001):

$$D_{AB} = \frac{(z_A + z_B) D_A D_B}{z_A D_A + z_B D_B} \tag{16}$$

where $z_A$ and $z_B$ are the charge numbers of ions $A$ and $B$, respectively. Finally, the nuclei size is taken to be the critical particle size, given by the following equation:

$$L_c = \frac{4\gamma_{CL} V_m}{\nu k T \ln S} \tag{17}$$

The kinetics used in the present work are the same as in Tang et al. (2022), and the reader may refer to that work for further details. Table 1 summarises the values of the kinetic parameters.

**Table 1**
Kinetics parameters of $BaSO_4$ precipitation at 25 °C.

| | Parameter | Value | Ref. |
|---|---|---|---|
| $D_{AB}$ | Apparent diffusion coefficient | $9.46 \cdot 10^{-10}$ m$^2$/s | (Mersmann, 2001) |
| $K_{SP}$ | Solubility product | $9.83 \cdot 10^{-11}$ kmol$^2$m$^2$ | (Monnin, 1999) |
| $K_{IP}$ | Equilibrium constant of $BaSO_4$(aq) ion pair formation | $5.4 \cdot 10^{-3}$ | (Monnin, 1999) |
| $K_{dis}$ | Dissociation constant between ions $HSO_4^-$, $H^+$ and $SO_4^{2-}$ | $1.2 \cdot 10^{-2}$ | (Schwarzer and Peukert, 2004b) |
| $M$ | Molar mass | 233.38 kg/kmol | - |
| $Sh$ | Sherwood number | 2 | (Schwarzer and Peukert, 2004b) |
| $V_m$ | Molecular volume | $8.61 \cdot 10^{-29}$ m$^3$ | - |
| $\nu$ | Dissociation number | 2 | - |
| $\gamma_{CL}$ | Interfacial energy | 0.1181 J/m$^2$ | (Schwarzer and Peukert, 2004b) |
| $\rho_c$ | Crystal density | 4480 kg/m$^3$ | - |

## 4. Study of fluctuations down to Kolmogorov scale

### 4.1. Simulation setup

The case that will be investigated in the present study is the precipitation of $BaSO_4$ nanoparticles in a T-mixer, as investigated experimentally by Schwarzer et al. (2006). The configuration of the T-mixer is shown in Fig. 1. The concentrations $BaCl_2$ and $H_2SO_4$ are 0.5 kmol/m$^3$ and 0.33 kmol/m$^3$, respectively. Both inlets have equal flow rates, yielding the Reynolds number of 1135 in the mixing channel, corresponding to turbulent flow for this configuration (Telib et al., 2004).

The simulation employs a three-dimensional uniform Cartesian grid with 21 million cells, whose cell size is selected so as to resolve the Kolmogorov scale. For reference, the mixing channel of the T-mixer is aligned with the $z$-axis and the two inlets are along the $x$-axis direction, as indicated in Fig. 1. For boundary conditions, a Poiseuille flow profile is applied to the inlets, and convective boundary condition is applied at the channel exit. The PSD is discretised into 45 intervals in the particle size space using the composite grid proposed by Tang et al. (2020); in that work, convergence of the PBE grid for the problem of $BaSO_4$ precipitation was also demonstrated. In order to account for the dissolution of reactants in water, the transported species include five ion species, namely $Ba^{2+}$, $SO_4^{2-}$, $Cl^-$, $H^+$, $HSO_4^-$, as well as the product, $BaSO_4$. The simulation parameters are the same as in Tang et al. (2020). The reactants are injected once the flow is statistically steady.

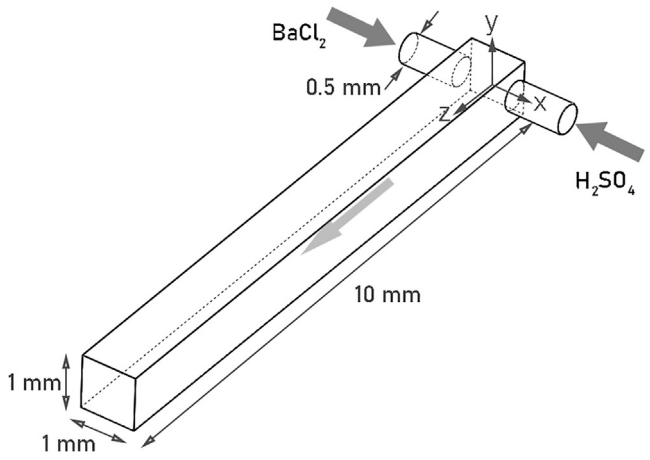


**Fig. 1.** Illustration of the T-mixer setup for the Schwarzer et al. (2006) (Re = 1135) case.

### 4.2. Main features of flow, mixing and PSD evolution in the T-mixer

The validation of the modelling approach has been carried out in our previous work (Tang et al., 2020), where the flow field was compared with PIV results from a scaled-up T-mixer due to Schwertfirm et al. (2007) while the exit PSD was compared with the experimental results of Schwarzer et al. (2006). The details of the comparison will not be repeated here, but the most important finding was that the simulated PSD at the exit was in good agreement with the experimental one, apart from a slight overprediction of the peak value. In the rest of the present section, we summarise some basic features of the flow and PSD evolution.

The flow from both inlets transitions to turbulent flow shortly after entering the mixing channel, as vortices are generated via the impinging jets. The mean flow in the impingement plane is shown in Fig. 2, which also shows an instantaneous distribution of an inert scalar entering from one of the inlets at the same plane to show the mixing environment in this zone, which is crucial for the induction of precipitation. Furthermore, a large helical vortex is formed at the centre of the channel and makes the velocity contour asymmetric; this is particularly evident in Fig. 3, which shows the mean streamlines. Apart from that, recirculations and secondary vortices are observed at two diagonal corners. These features define the global mixing environment and set the stage for the macro-, meso- and micromixing. Notably, the reactant entering on one side has to meet with the one entering on the other side through the outer part of the channel, and the thin boundaries between the two streams provide the interface in which precipitation is initiated. The helical flow structure increases the residence time in the impingement zone, making most of the reaction to occur there.

The evolution of the PSD at the centreline of the inlets along the $x$-direction and in the mixing channel along the $z$-direction is shown in Fig. 4. In both directions, a unimodal distribution can be

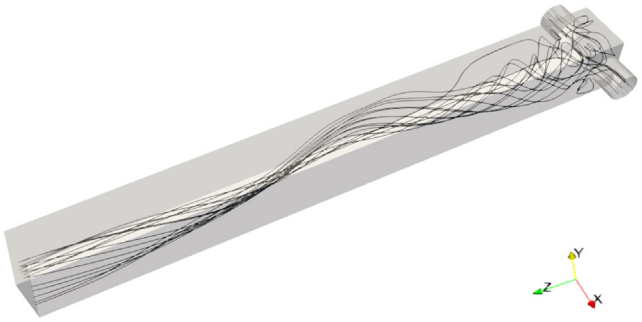


**Fig. 3.** Mean streamlines of the flow field.

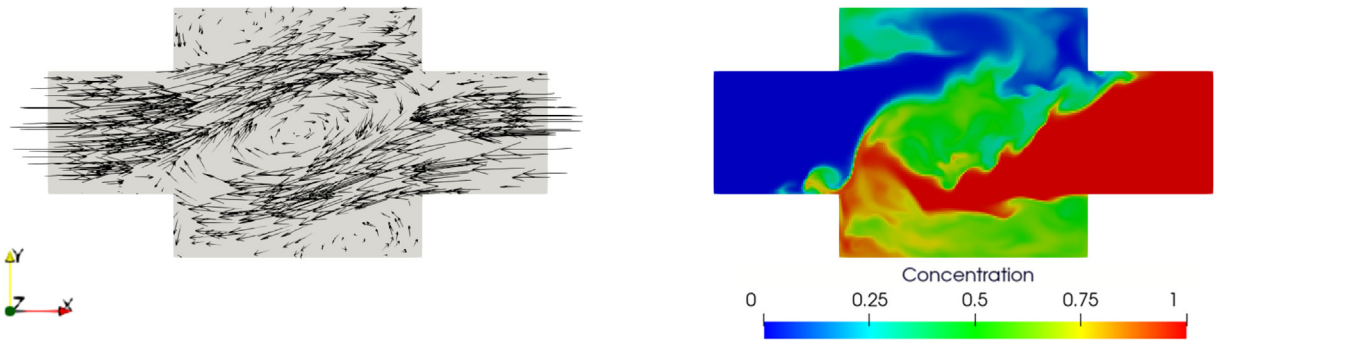


**Fig. 2.** Mean velocity vectors (left) and instantaneous contour plot of the concentration of a passive scalar entering from one of the inlets (right). The figures show the impingement zone.

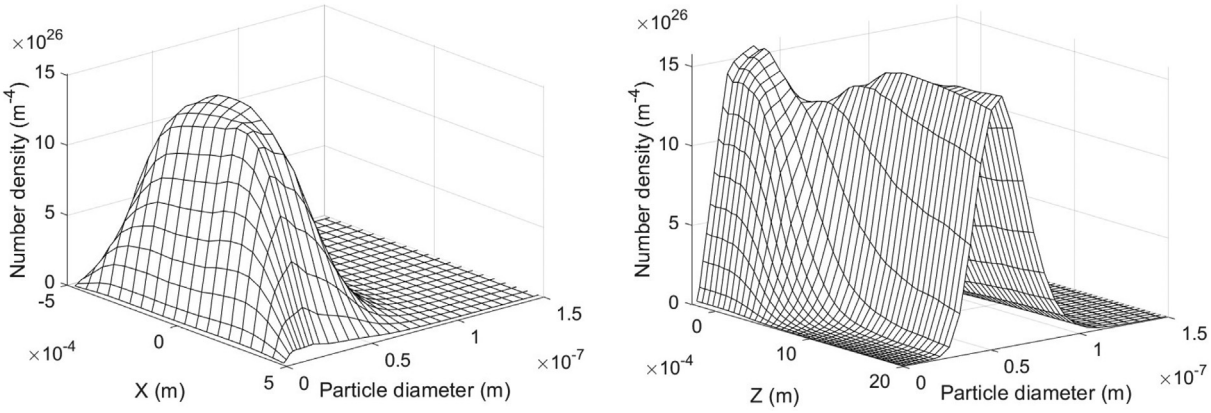


**Fig. 4.** Mean number densities in the x- (left) and the z- (right) direction.

clearly identified. Between the two inlets, the number of particles increases drastically at the impingement centre as a consequence of the mixing of the inlet streams and the nucleation incurred. At this stage, most of the particles are young and their size distribution peaks at around 30 nm. Along the mixing channel, the PSD exhibits a rapid shift in its peak location and reaches 50 nm in the first 1 mm of the channel. The peak and the width of the PSD do not exhibit significant changes beyond that point, indicating that most of the particle nucleation and growth have been completed. The focus of the investigation will therefore be on the effect of fluctuations within the upstream part of the T-mixer.

### 4.3. Fluctuations in supersaturation, nucleation and growth rates

We first examine the impact of fluctuations on the nucleation and growth rates. As mentioned in Section 2.2, this will be accomplished by computing the difference between the mean rates (as computed by DNS) and the rates computed using the mean composition, i.e. $\langle B\rangle - B(\langle C_1\rangle, \ldots, \langle C_m\rangle)$ and $\langle G\rangle - G(\langle C_1\rangle, \ldots, \langle C_m\rangle)$. These differences are important because the objective of precipitation models is to obtain a closed formulation of the problem in terms of the mean concentrations, particle number density and fluid velocity. We also compute the supersaturation in both ways (i.e. $\langle S\rangle$ and $S(\langle C\rangle)$), since both the nucleation and the growth rate are functions of supersaturation.

The mean supersaturation contours in the x-y and x-z planes are shown in Fig. 5. The typical pattern that results from the helical vortex is observed on the x-y plane. Yet, the region of high supersaturation covers a wider area when computed with the mean values, while the maximum magnitude is overpredicted by 14%, indicating more rapid reactant consumption. As can be seen from Eq. 12, supersaturation is proportional to the square root of the product of reactant concentrations, and this non-linearity is responsible for these differences. Since the growth rate is a linear function of supersaturation (Eq. 14), the contours of the two quantities are the same and not shown; both quantities share also the same overprediction.

Fig. 6 shows the nucleation rate contours. An overprediction of the nucleation rate is evident when computed with the mean concentrations, with the maximum being 50% overestimated. This difference indicates that the non-linear dependence of nucleation on supersaturation amplifies the discrepancy in the

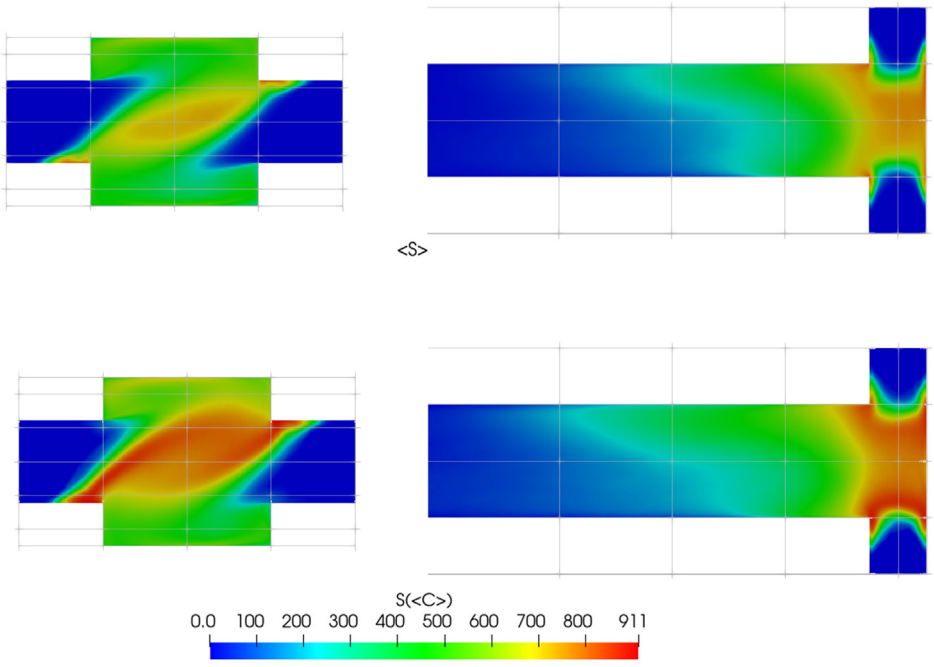


**Fig. 5.** Mean supersaturation (top) and supersaturation obtained from mean concentration (bottom).

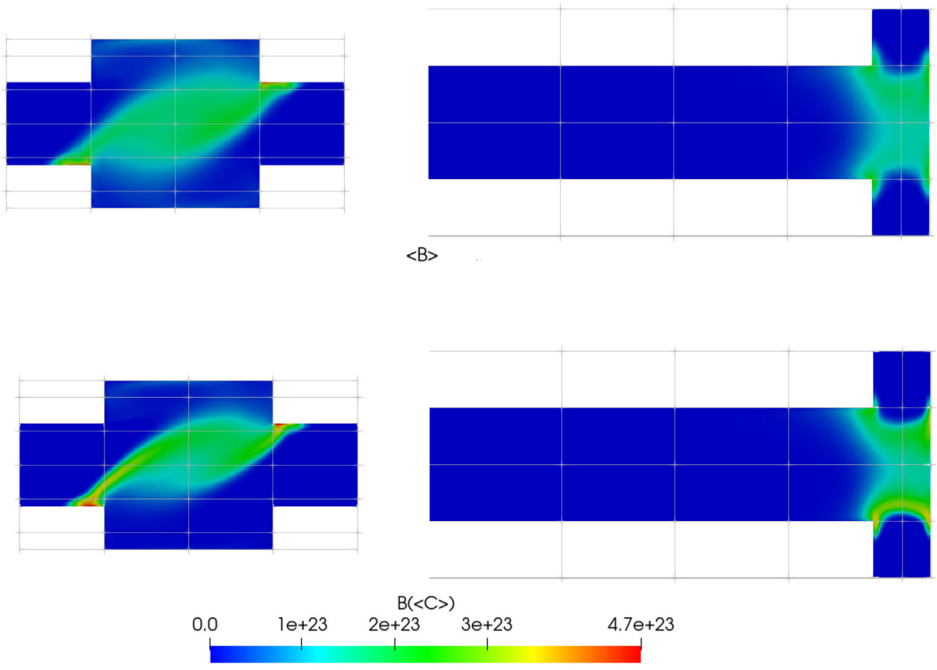


**Fig. 6.** Mean nucleation rate (top) and nucleation rate obtained from mean concentration (bottom).

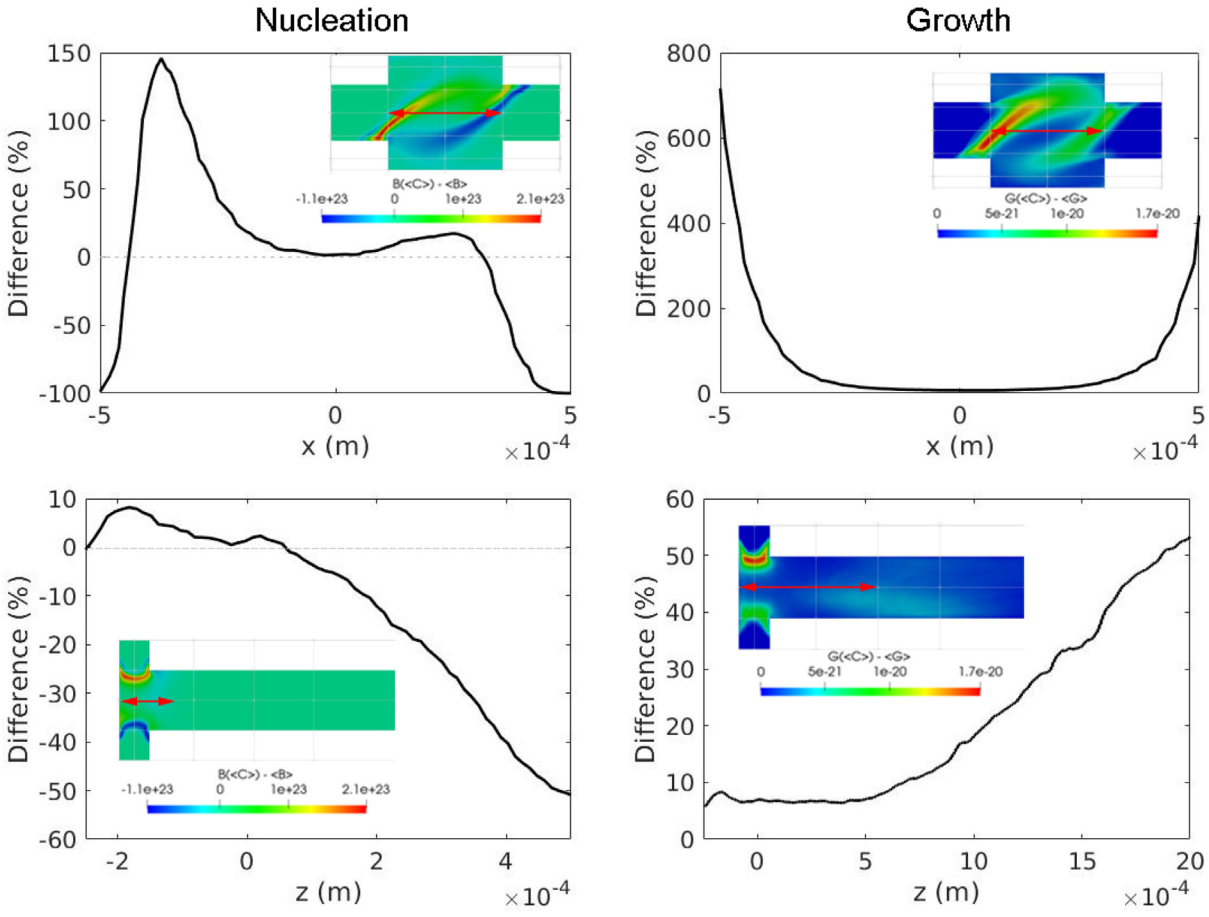


**Fig. 7.** Percentage difference between the rates computed with mean values and the DNS means across the centreline of the impingement zone in the x-direction (left) and along the centreline of the mixing channel in the z-direction (right). The differences are calculated as $(B(\langle C\rangle) - \langle B\rangle)/\langle B\rangle$ and $(G(\langle C\rangle) - \langle G\rangle)/\langle G\rangle$, respectively.

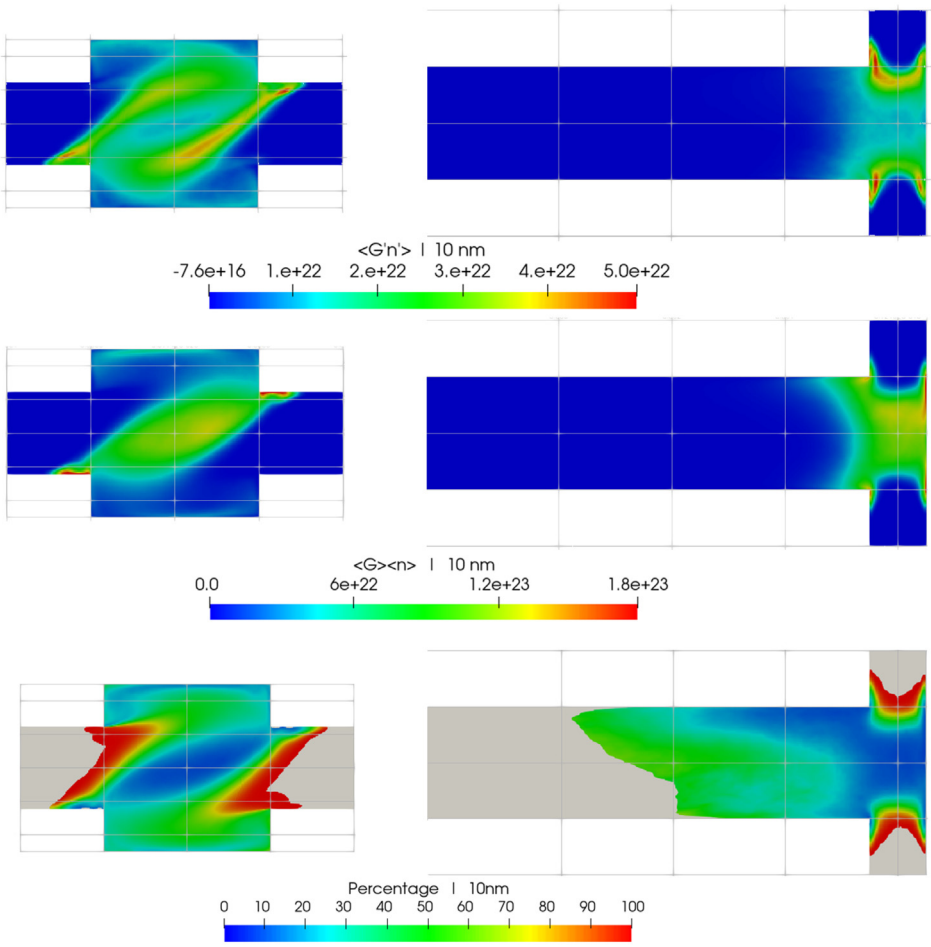


**Fig. 8.** Number density-growth rate correlations, $\langle G'n' \rangle$ (top), and product of mean growth rate and mean number density, $\langle G \rangle \langle n \rangle$ (middle), at 10 nm. The bottom figure shows the percentage contribution of $\langle G'n' \rangle$ to the total mean, $\langle Gn \rangle$.

nucleation rate. One interesting observation here is that, while the mean-based supersaturation covers a wider area of the impingement zone than the DNS-computed mean, the reverse is observed with nucleation. This is likely because of the intermittent characteristics of nucleation, which occurs via short bursts. The study of Tang et al. (2022) showed that the local nucleation bursts contribute to the majority of the local mean, as it was found that the nucleation rate is very weak in most other instances during the simulation. However, the high values of instantaneous concentrations that trigger nucleation bursts are averaged out in the mean concentration field. As a result, the calculation with the mean concentrations can result in overprediction of the maximum nucleation rate while still underpredicting the number of nuclei.

The percentage difference between DNS and mean-based rates across the impingement zone and along the channel is shown in Fig. 7[1]. Significant differences are observed at both ends of the impingement zone, where the two curves diverge and the nucleation rate features both underpredictions and overpredictions by the mean-based model, while the growth rate is overpredicted, consistent with Figs. 5 and 6. The overshoot or undershoot can reach 100% or more at the region of strong precipitation. The two ends are indicative of the impingement of the two jets and the onset of the formation of the helical vortex, and Fig. 5 also shows that supersaturation exhibits a large discrepancy when computed via the means in that region. A difference between the behaviours of nucleation and growth is also observed and even magnified in $z$-direction, where the modelled mean nucleation rate again appears to be underestimated while the growth rate is overestimated.

It must be noted that the mean-based prediction is not indicative of the performance of a RANS model, because the mean concentrations in this case have been computed from the DNS results and are not subject to the RANS model assumptions. Further discrepancies can be expected when a RANS model is used, but the objective of this study is to isolate the effect of turbulent fluctuations.

### 4.4. Particle number density - growth correlations

#### 4.4.1. Investigation of $\langle G'n' \rangle$

We now turn our attention to the particle number density - growth correlations, $\langle G'n' \rangle$, which manifests itself through the gradient $\frac{\partial \langle Gn \rangle}{\partial v}$. In the present section, we examine $\langle G'n' \rangle$ on its own, while its gradient and contribution to the source term will be investigated in the following sections. As this correlation is a function of particle size, we look at the correlation in the discretised equation, $\langle G_k n'_k \rangle$, for three representative particle size intervals, namely 10 nm, 50 nm and 80 nm, indicative of the low, medium and high particle size ranges, respectively.

Figs. 8–10 show the correlation contours, $\langle G'n' \rangle$, together with the product of mean growth rate and mean number density, $\langle G \rangle \langle n \rangle$, in the x-y and x-z plane at the selected intervals. The per-

[1] It must be noted that, since growth is a linear function of particle diameter (as can be shown from Eqs. 14 and 15), the difference calculated here is the same for all diameters.

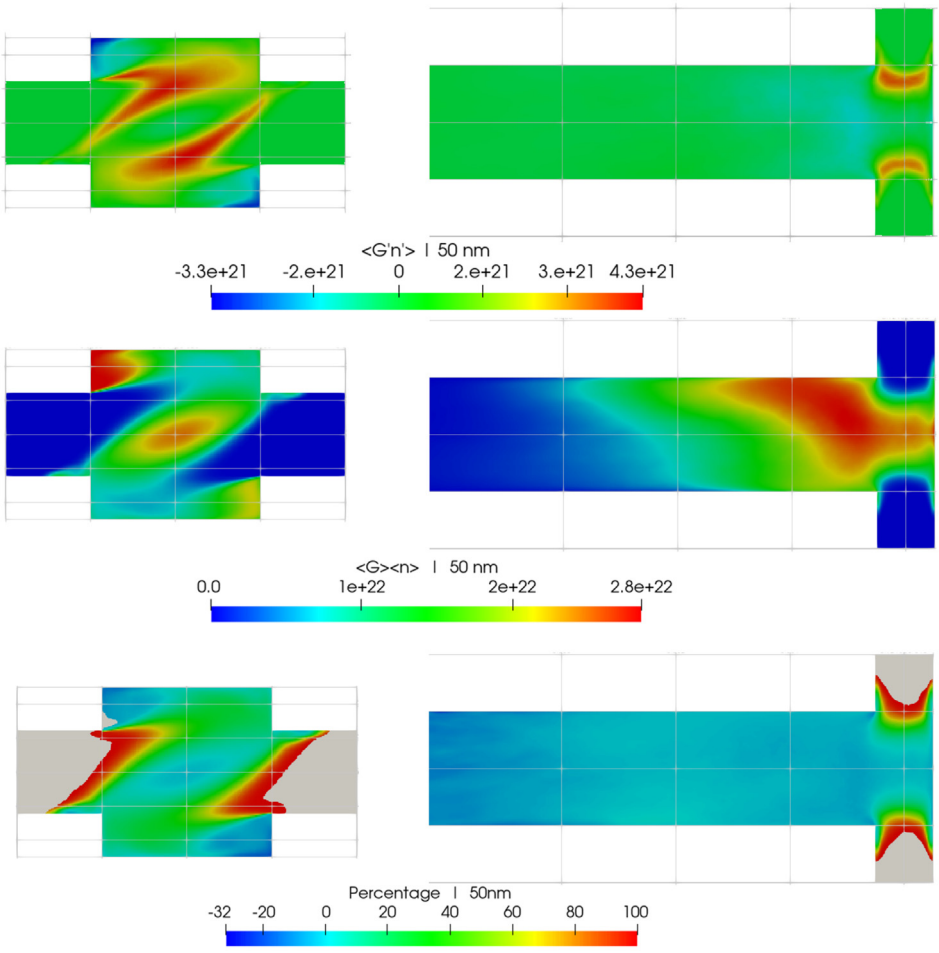


**Fig. 9.** Number density-growth rate correlations, $\langle G'n' \rangle$ (top), and product of mean growth rate and mean number density, $\langle G \rangle \langle n \rangle$ (middle), at 50 nm. The bottom figure shows the percentage contribution of $\langle G'n' \rangle$ to the total mean, $\langle Gn \rangle$.

centage contribution of $\langle G'n' \rangle$ to $\langle Gn \rangle$ is also shown. The correlations are strongest at the stream boundaries and recirculation corners, whereas the mean product term, $\langle G \rangle \langle n \rangle$, peaks at the helical vortex centre. The correlation terms contribute considerably to $\langle Gn \rangle$ in the impingement zone, with typical values of 50–70% at 10 nm and 20–40% at the other two intervals. Apart from that, their magnitude varies not only with location, but also with particle size: both the mean product terms and the correlation terms are much stronger at small intervals due to the stronger growth rate at small particle sizes (see Eq. 14). This leads to diminishing number density - growth correlations in the particle size domain and has vital implications for the gradient of $\langle G'n' \rangle$, which will be further discussed in Section 4.4.2.

Regarding the sign of the $\langle G'n' \rangle$ term, both positive and negative correlations are observed. Before giving an explanation of this, we first need to understand that fluctuations in growth alone would bring out a negative correlation. This is because the growth rate 'convects' number density to larger intervals and, since the latter is defined as number of particles divided by particle size, a fluctuation involving an increased growth rate would move more particles to bigger sizes and result in lower number densities, while the reverse would occur for a one with a decreased growth rate. Yet, when nucleation is introduced, it acts as a source of number density at the smallest size. Strong positive correlations appear at the stream boundaries of the helical vortex where a rotational 'double dolphin' pattern can be seen from the x-y plane. The location of these patterns is where high RMS of supersaturation (and therefore growth rate) was found, and furthermore highly intermittent nucleation rates were observed in the analysis of Tang et al. (2022). The intense nucleation bursts are therefore believed to be the cause of the strong positive correlations: the number densities at the smaller end of the distribution drastically increase and propagate to the larger end during nucleation bursts, thus counterbalancing the effect of growth. Evidence of this explanation can be found from Fig. 11, where all correlation pairs along the channel centrelines at x- and z-direction are shown. In both directions, the correlation terms remain positive for intervals below the PSD peak (see Fig. 4) with magnitude reducing with size. It is also worth mentioning, that along the z-direction, while the correlation at small intervals stays positive, the magnitude suddenly drops after 0.4–0.5 mm. This is approximately the starting point of the growth dominant zone as identified in Tang et al. (2022), suggesting that the growth mechanism takes over the process, suppressing the nucleation contribution from that point onwards.

By contrast, strong negative correlations concentrate at the recirculation zones at diagonal corners (in the 50 nm and 80 nm contours). Compared to its positive counterpart, the negative correlation is negligible at small sizes but its magnitude becomes higher at larger sizes. This is evidenced by the magnitude ratio of the maximum negative-to-positive correlation that rises from

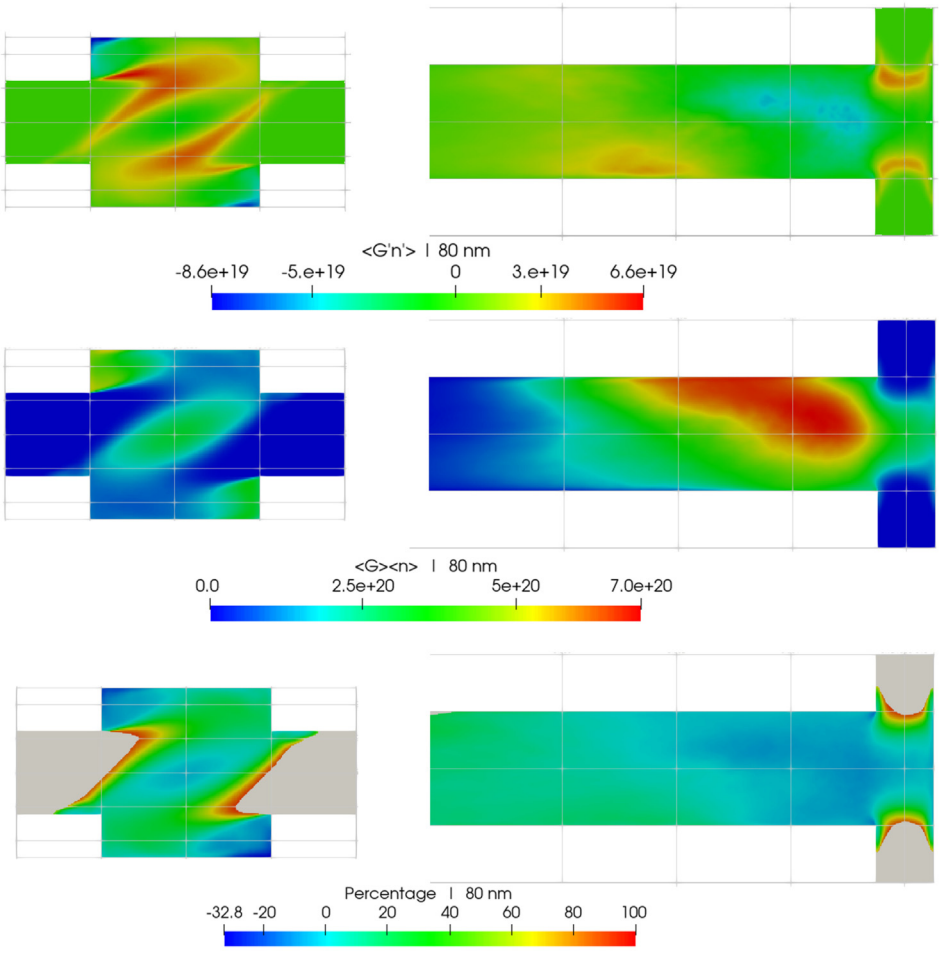


**Fig. 10.** Number density-growth rate correlations, $\langle G'n' \rangle$ (top), and product of mean growth rate and mean number density, $\langle G \rangle \langle n \rangle$ (middle), at 80 nm. The bottom figure shows the percentage contribution of $\langle G'n' \rangle$ to the total mean, $\langle Gn \rangle$.

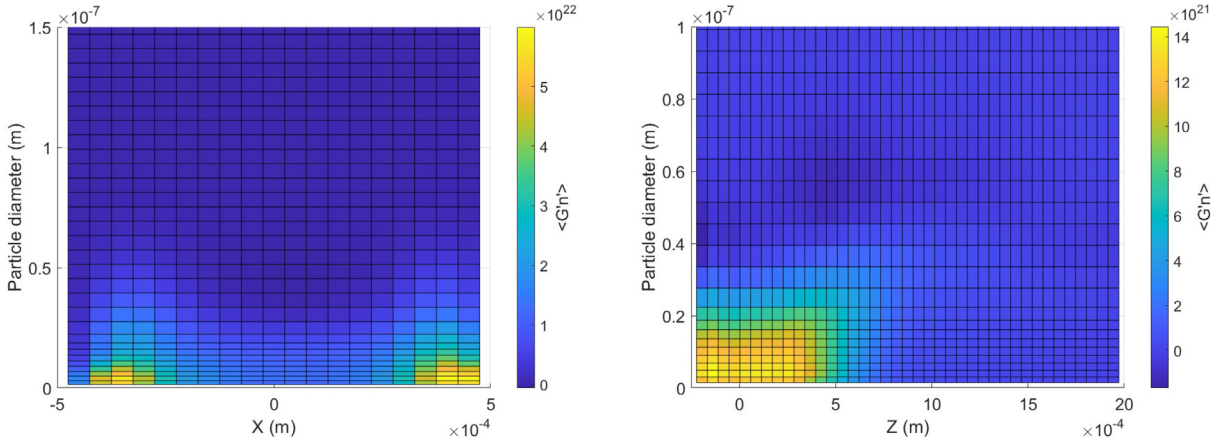


**Fig. 11.** $\langle G'n' \rangle$ correlations of all intervals across the channel entrance passing through impingement centre (left) and along the $z$-direction (right).

$1.52 \cdot 10^{-6}$ at 10 nm to 1.30 at 80 nm. The maximum negative correlations are found at the mixer corners that overlap with the secondary vortices, which we believe to be due to a combination of strong growth and weak nucleation, which results in a relocation of particles to bigger sizes that is not balanced by nucleation. This is also in accordance with the findings of Tang et al. (2022), where nucleation was found to be very weak in these corners.

#### 4.4.2. Investigation of $\partial \langle G'n' \rangle / \partial v$

The number density-growth rate correlations contribute to the averaged PBE (Eq. 8) through the growth term, which appear as a gradient term in the particle size domain and can be broken down into mean and fluctuating parts. The x-y and x-z contours of the fluctuation ($\frac{\partial \langle G'n' \rangle}{\partial v}$) and mean ($\frac{\partial \langle G \rangle \langle n \rangle}{\partial v}$), as well as the percentage contribution from the fluctuating part to the total growth term ($\frac{\partial \langle Gn \rangle}{\partial v}$) at

the selected size intervals are shown in Figs. 12, 13 and 14. Sharp changes (red and blue lines) appear in the percentage contours at 10 nm and 50 nm intervals (Figs. 12 and 13) because of the changing sign and zero-crossing of the sum ($\frac{\partial\langle G\rangle\langle n\rangle}{\partial v}+\frac{\partial\langle G'n'\rangle}{\partial v}$). To avoid extreme values due to division by a small number and for better visualisation, the color scales in the contours have been limited to $\pm150\%$ and $\pm100\%$, respectively.

In the three selected size intervals, both the mean and fluctuation terms are negative in most regions because the $\langle G'n'\rangle$ and $\langle G\rangle\langle n\rangle$ terms were previously found to reduce with increasing particle size (Section 4.4.1). Comparing with the total growth term, the fluctuation contributions at the small size intervals are more significant than at the larger sizes, as was the case with $\langle G'n'\rangle$. As the total growth term in the entire distribution is considerably underestimated without the fluctuation terms, this has two consequences that could result in considerable deviations in the PSD prediction if fluctuations were neglected. Firstly, since the percentage contribution indicates a larger amount of underestimation of the growth at smaller particle sizes, the particle number at the lower end of the distribution would be overpredicted. This would cause the PSD shape to skew towards the lower end of the distribution. Secondly, owing to the underestimated crystal volume, and hence the consumption histories, the supersaturation build-up would be affected and the kinetic rates predicted would be incorrect too. Particle growth is the terminating step in precipitation and, therefore, less consumption due to growth would result in more nucleation, thus skewing the PSD towards smaller sizes.

#### 4.4.3. Investigation of the integral of $v\partial\langle G'n'\rangle/\partial v$ in the source term

Finally, we evaluate the fluctuation contribution to the consumption term in reactant transport (Eq. 10). The magnitude of this contribution is found to be very small, hence Fig. 15 shows only its percentage contribution to the mean consumption ($-\int v\frac{\partial\langle Gn_k\rangle}{\partial v}dv$). Note that these terms appear in the reaction source $R_\alpha$ in Eq. 2, hence the negative sign in the front.

The fluctuation contribution to growth consumption rate contains both positive and negative regions. Positive contributions can be found at the stream boundaries, whereas negative correlations concentrate at the diagonal corners and at the centre of the mixing channel. The contours share a similar pattern to the PBE growth terms (cf. Section 4.4.2). In comparison with the mean consumption, similar to what was found in Section 4.4.1 about the correlation terms, $\langle G'n'\rangle$, the location of negative fluctuations overlaps with regions of high consumption. As a considerable amount of fluctuations was observed in the growth term of the PBE (cf. Section 4.4.2), the small values in the integral signify that positive and negative fluctuations at different sizes cancel out. To show this, the fluctuating part of the consumption is broken down to the contributions at each size interval. That is, the integral evaluated within each size interval, namely $\int_{v_{k-\frac{1}{2}}}^{v_{k+\frac{1}{2}}} v\frac{\partial\langle G'n'_k\rangle}{\partial v}dv$, is examined.

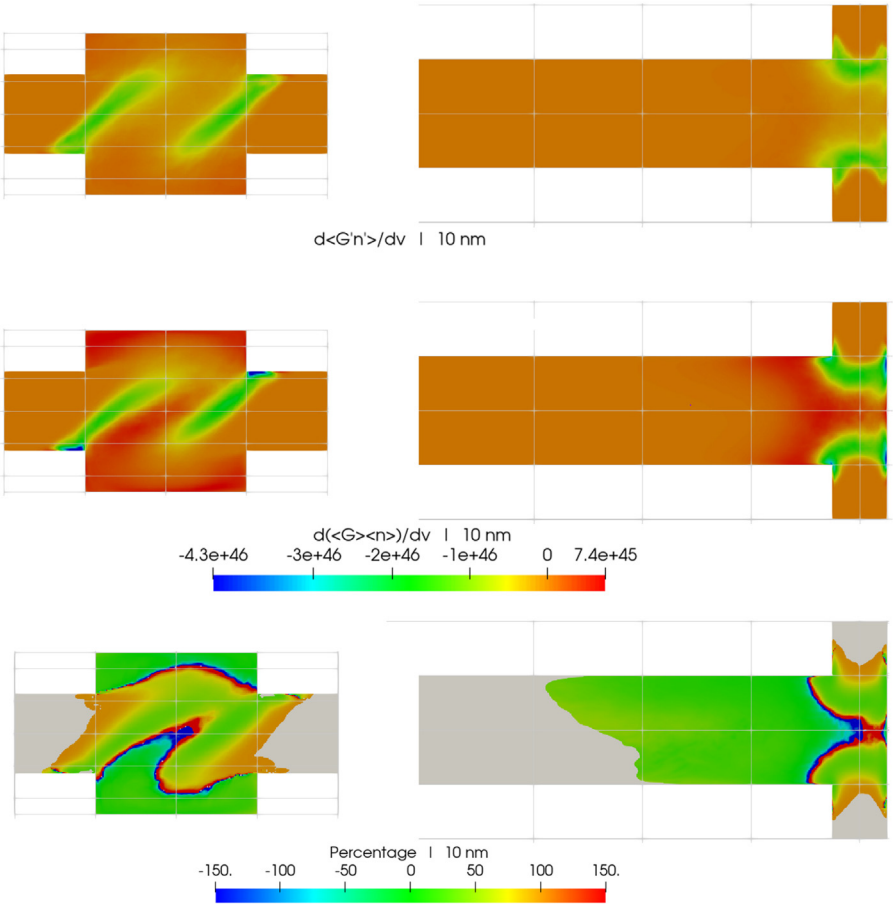


**Fig. 12.** The fluctuating part, $\frac{\partial\langle G'n'\rangle}{\partial v}$ (top), and mean, $\frac{\partial\langle G\rangle\langle n\rangle}{\partial v}$ (middle), of particle growth in the PBE at 10 nm, respectively. The bottom figure shows the percentage contribution of $\frac{\partial\langle G'n'\rangle}{\partial v}$ to the total mean, $\frac{\partial\langle Gn\rangle}{\partial v}$.

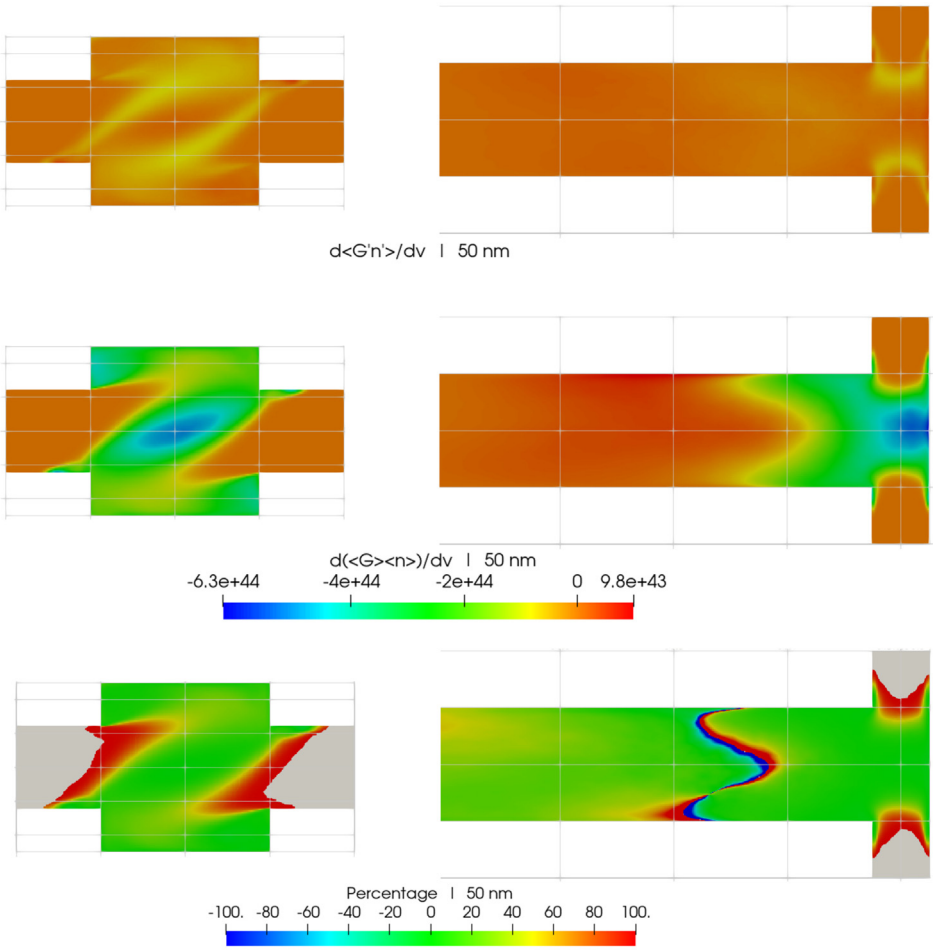


**Fig. 13.** The fluctuating part, $\frac{\partial\langle G'n'\rangle}{\partial v}$ (top), and mean, $\frac{\partial\langle G\rangle\langle n\rangle}{\partial v}$ (middle), of particle growth in the PBE at 50 nm, respectively. The bottom figure shows the percentage contribution of $\frac{\partial\langle G'n'\rangle}{\partial v}$ to the total mean, $\frac{\partial\langle Gn\rangle}{\partial v}$.

The contribution from each interval along the centreline of x- and z-axis is shown in Fig. 16. Similar to the individual growth terms in Figs. 12–14, the map shows that the amount of consumption in each size intervals varies. The positive elements and their negative counterparts have comparable magnitudes, which offset and balance each other in the integral of all intervals, leading to very small fluctuation contribution in the consumption term.

## 5. Study of fluctuations of sub-Kolmogorov scale

The results so far were based on the $Sc = 1$ assumption. This was based on a hypothesis that the excessive diffusion given by $Sc = 1$ to some extend compensates for the effect of the unresolved sub-Kolmogorov scales that appear at high $Sc$. Although comparison with experiments (Tang et al., 2020) showed that the exit PSD agreed to an acceptable accuracy, we wish to further examine the validity of this hypothesis. In the present section, therefore, an attempt is made to identify the effects arising from mixing at sub-Kolmogorov scales on the precipitation process via a new simulation conducted with both $Sc = 1$ and 10. In particular, we will investigate the effects on the distribution of reaction zones, reaction rates and PSD. It must be emphasised that the present work serves as a preliminary study of identifying the contribution from the Schmidt number in liquid phase reacting flows, since it is still not possible to resolve the Batchelor scale at a Schmidt number of the order of 1000.

### 5.1. Simulation setup

The simulations performed for this study are conducted on a T-mixer similar to the one in the precipitation experiment simulated in Section 4. In order to identify the contributions from the grid resolution and Schmidt number, the same simulation is performed under different Schmidt number conditions and grid resolutions. A few changes on the operating conditions and on the reactor geometry, however, were made to make the simulations possible on presently available computation hardware.

The first modification is on the Reynolds number, which is reduced to 400 in the mixing channel; this is the highest possible Reynolds number that can be reached with our computational resources so as to ensure turbulent flow in a T-mixer (Telib et al., 2004) while resolving the Batchelor scale by maintaining the maximum cell-size-to-$\eta_c$ ratio to 2 at an elevated Schmidt number of 10.

Apart from that, the reactor simulated is of the same size as the one used in Section 4 in terms of the channel and inlet width, but with some modifications to reduce the number of cells required. The differences are that the mixer length is chosen to be only 30% of the one considered in Section 4, since most of the precipitation has been found to occur at the impingement and the upstream of the mixing channel. In addition, the cross-section of the inlets is changed to a square duct in order to have a higher degree of con-

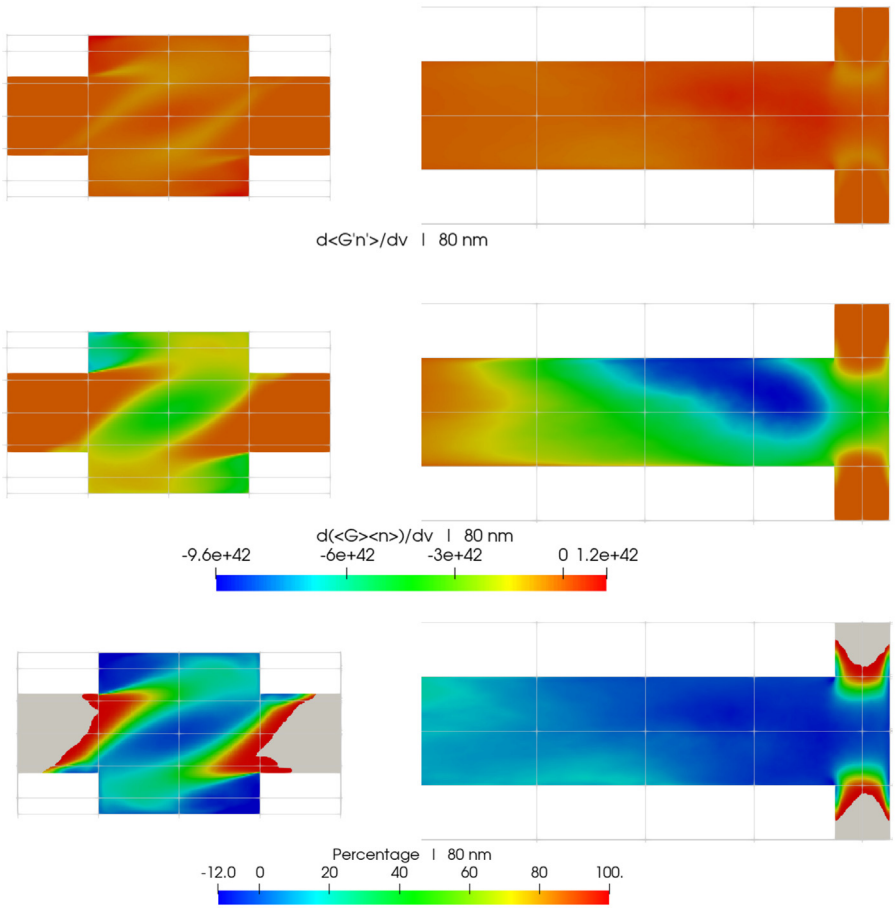


**Fig. 14.** The fluctuating part, $\frac{\partial\langle G'n'\rangle}{\partial v}$ (top), and mean, $\frac{\partial\langle G\rangle\langle n\rangle}{\partial v}$ (middle), of particle growth in the PBE at 80 nm, respectively. The bottom figure shows the percentage contribution of $\frac{\partial\langle G'n'\rangle}{\partial v}$ to the total mean, $\frac{\partial\langle Gn\rangle}{\partial v}$.

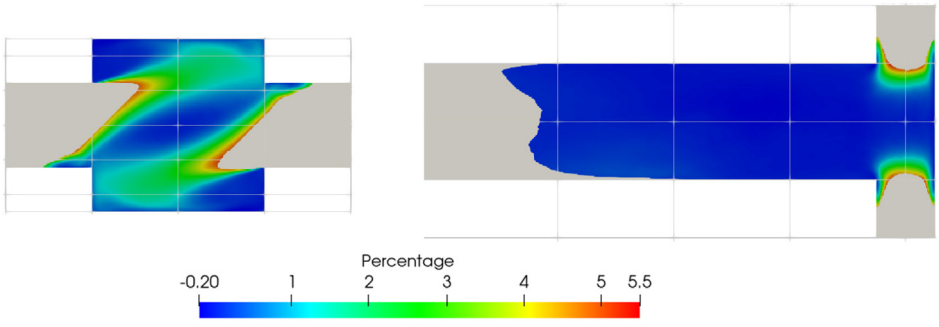


**Fig. 15.** The percentage contribution from the fluctuations, $-\int v\left(\frac{\partial\langle G'n'\rangle}{\partial v}\right)dv$ (top), to the total mean species consumption due to particle growth, $-\int v\left(\frac{\partial\langle Gn\rangle}{\partial v}\right)dv$ (middle).

formality with a Cartesian grid. The simulation setup is shown in Fig. 17.

Two grids were prepared for this investigation; they are called 'fine' and 'medium' resolution in the present section and feature a smallest cell size, $\Delta x$, of $4\cdot10^{-6}$m and $8\cdot10^{-6}$ m respectively. This way, both grids have adequate resolution to resolve the Kolmogorov scale, but the fine resolution grid is also able to resolve the Batchelor scale at $Sc = 10$. In order to reduce the number of cells in the grid, stretching is applied along the downstream of the mixing channel and the inlets, making the resolution finer in the impingement zone. This amounts to 15 and 6 millions of cells in the fine and medium resolution grids, respectively. A summary of the grid resolutions and their ratio with the Kolmogorov and Batchelor scales is shown in Table 2.

Three simulations have been performed: $Sc = 1$ at medium resolution and $Sc = 10$ at both medium and fine resolutions. In the medium resolution, the $Sc = 1$ case is akin to the simulations shown in Section 4, whereas the $Sc = 10$ case is an under-resolved (with respect to the Batchelor scale) but still high $Sc$ simulation. On the other hand, the simulation at high resolution and $Sc = 10$ resolves the Batchelor scale. As in the previous simulations, the reactants are injected once the flow statistics are steady,

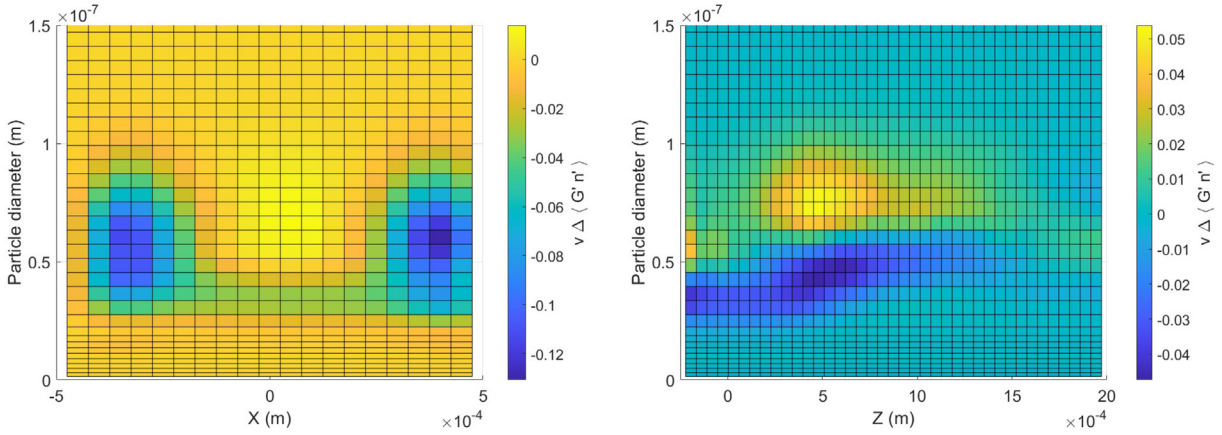


**Fig. 16.** The integral $\int_{v_{k-\frac{1}{2}}}^{v_{k+\frac{1}{2}}} v \frac{\partial \langle G' n'_v \rangle}{\partial v} dv$ from each size interval at x-(left) and z-(right) direction.

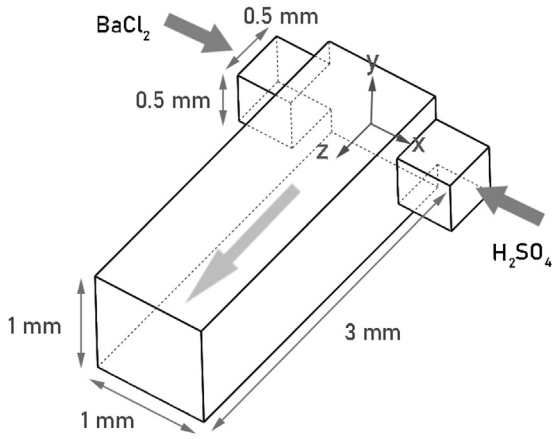


**Fig. 17.** Illustration on the process setup for the Re = 400 case.

**Table 2**
Grid sizes.

| | Medium resolution | Fine resolution |
|---|---|---|
| Smallest cell size | $8 \cdot 10^{-6}$ | $4 \cdot 10^{-6}$ |
| Number of cells | 6 million | 15 million |
| $\Delta x/\eta$ | 1.36 | 0.68 |
| $\Delta x/\eta_c$ ($Sc = 10$) | 4.30 | 2.14 |

while the mean particle size distributions is collected after 15 flow-through times.

### 5.2. Structure of reaction zones

In reacting flows, the diffusivity often affects the size of reaction zones, which in turn may have an impact on species consumption. The present section attempts to compare the reaction zones at $Sc = 1$ and $Sc = 10$ and examine the effect of grid resolution.

To examine the extent of reaction zones, the iso-surfaces of the nucleation and growth consumption rates were extracted at 30 uncorrelated time instances and at 20%, 50% and 70% of their maximum time-averaged consumption rate in the entire domain. Figs. 18 and 19 show an instantaneous snapshot of the iso-surfaces for nucleation and growth, respectively. By comparing the iso-surfaces at $Sc = 1$ and $Sc = 10$ (fine resolution), we observe that the latter shows finer structures in the reaction regions of both nucleation and growth. In all cases, the extent of the reaction zones decreases at increasing percentage; at the highest percentage, intense consumption is found only at the impingement. The changes in the growth iso-surfaces are more noticeable than in the nucleation ones because growth extends further into the mixing channel.

The iso-surfaces can be quantified by their surface area, while time-averaging is performed on the 30 time instances. The time-averaged iso-surface area at the corresponding percentages are presented in Table 3 and 4 for nucleation and growth, respectively, and both are normalised by the mixing channel cross-sectional area. A few observations can be made from the comparison of mean iso-surface areas. By comparing the three cases, the mean iso-surface area for both nucleation and growth at all percentages is considerably higher at $Sc = 10$ compared to $Sc = 1$. This confirms the formation of thinner and finer patterns expected at high Schmidt number flows. A considerable difference is also found between the fine and medium resolutions at $Sc = 10$. This deviation can go up to 24% in nucleation and 33% in growth in the iso-surface of intense reaction (70% of the maximum), but still not as much as in the medium resolution $Sc = 1$ case.

### 5.3. Effect of Schmidt number on precipitation rates

Having some preliminary understanding of the extent of reaction zones, the present section looks into the effect of $Sc$ on the precipitation rates. In particular, we wish to answer the questions of whether a thinner reaction zone at higher Schmidt number would lead to different nucleation and growth rates and how the PSD would be thus affected. To proceed, the local mean nucleation and growth consumption rates are integrated throughout the reactor to compute a volume-averaged mean reaction rate for the entire domain. Table 5 lists the volume-averaged mean nucleation and growth consumption rates in the reactor from the each of the three cases investigated. Surprisingly (given the considerable differences observed in the iso-surface contours), the differences here are small, suggesting that the total consumption rate for each of the two crystallisation mechanisms is very similar. In order to find an explanation for this observation, we examine the consumption rate contours, where we can find clues about the competing effects between the local reaction rates and the reaction zone coverage. Fig. 20 shows the instantaneous contours of supersaturation, nucleation consumption rate and growth consumption rate at Schmidt numbers of 1 and 10 (fine resolution). The contours exhibit

similar characteristics as in the previous simulations, and a helical vortex is also obtained. Both nucleation and growth contours follow the supersaturation pattern, but the former is present in thinner zones, as has been discussed in the previous section. In the comparison between the contours at $Sc = 1$ and $Sc = 10$, the main features are essentially the same, but the contours at $Sc = 1$ have much wider coverage in the kinetics and consumption rates. This observation is in agreement with the study of Derksen (2012) on inert scalar mixing in stirred tanks. Apart from the coverage, one important difference between the two Schmidt number conditions is that the maximum rates in the $Sc = 1$ case are lower compared with $Sc = 10$. That is, the low $Sc$ case has wider coverage but lower reaction rate and opposite in the high $Sc$ case. It appears that the coverage of reaction zones competes with the magnitude of the local reaction rate in the Schmidt number range under consideration and, as a result, both cases contribute to similar amount of consumption in the system. The overall trend therefore suggests that, at elevated Schmidt number, reactions are confined to thinner zones and larger iso-surface area, in which greater local rates of consumption and kinetics arise.

### 5.4. Effect of Schmidt number on the particle size distribution

We now turn our focus on the differences in the resultant particle size distributions between $Sc = 1$ and $Sc = 10$. The time- and plane-averaged PSD at the exit is extracted in each case and the results are presented in Fig. 21. The PSDs from the three cases show no major differences in terms of the shape and peak location. In particular, the fine and medium resolution cases give almost identical distribution at $Sc = 10$. This can be attributed, to a large extend, to the very small differences in the nucleation and growth consumption rates. The present comparison, therefore, suggests that the effect of grid resolution on the PSD in this case is small as long as the Kolmogorov scales are captured. The Schmidt number used in the simulation appears to play a secondary role on the PSD prediction. In particular, the high Schmidt number results from the under-resolved grid is virtually identical to the same distribution by the fine resolution simulation. Additionally, despite the small deviations in the PSD from the $Sc = 1$ and $Sc = 10$ cases, the comparison shows that, overall, the PSD at lower $Sc$ is marginally biased towards the larger sizes: the number density at large intervals are slightly higher whereas the peak number density is slightly lower. This observation can be accounted for by the presence of larger but fewer particles in the PSD at low Schmidt number condition, as evidenced in the time-and-plane-averaged moments evolution along the channel in Fig. 22. However, the effect is relatively small. It must also be noted that the TVD scheme may take over the diffusion in a form of numerical error when a very high $Sc$ is used in an under-resolved grid and thus further increase in Schmidt number may not improve the solution.

It can be seen from the zeroth moment that, overall, more nuclei are formed throughout the process at $Sc = 10$ despite the lower number of particles at the impingement. Still, the number of particles in the $Sc = 10$ case exceeds that in the $Sc = 1$ case at

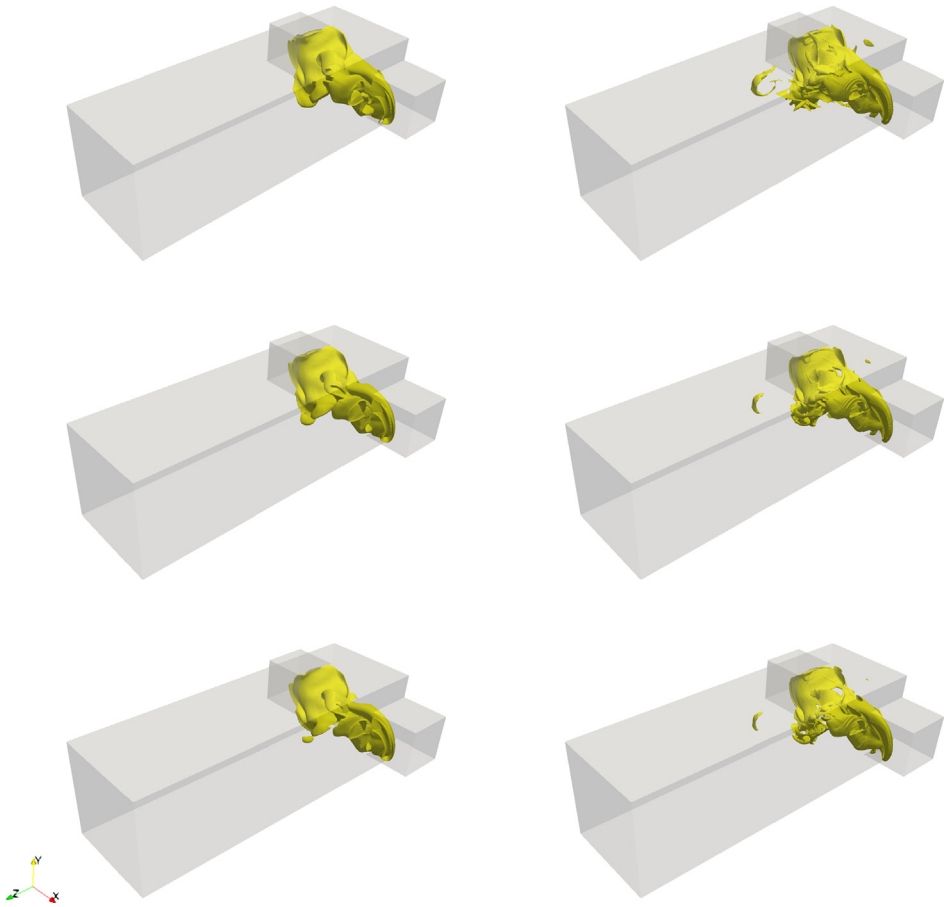

**Fig. 18.** Iso-surface of instantaneous nucleation consumption rate at 20% (top), 50% (middle) and 70% (bottom) of the maximum at Schmidt number 1 (left) and 10 in the fine resolution (right).

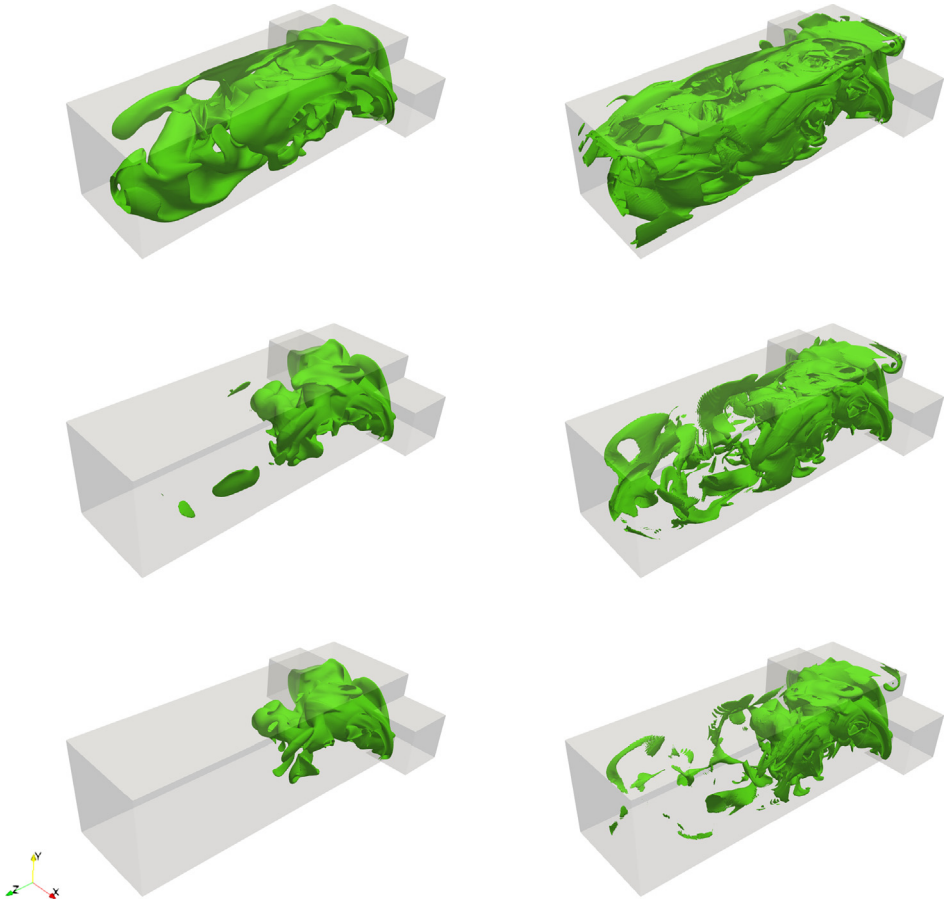

**Fig. 19.** Iso-surface of instantaneous growth consumption rate at 20% (top), 50% (middle) and 70% (bottom) of the maximum at Schmidt number 1 (left) and 10 in the fine resolution (right).

**Table 3**
Mean iso-surface area of the nucleation consumption rate (dimensionless, normalised by the mixing channel cross-sectional area).

| Case/ percentage | 20% max | 50% max | 70% max |
|---|---|---|---|
| Medium, Sc = 1 | 4.99 | 3.78 | 3.20 |
| Medium, Sc = 10 | 7.63 | 5.84 | 5.17 |
| Fine, Sc = 10 | 9.86 | 7.67 | 6.81 |

**Table 4**
Mean iso-surface area of the growth consumption rate (dimensionless, normalised by the mixing channel cross-sectional area).

| Case/ percentage | 20% max | 50% max | 70% max |
|---|---|---|---|
| Medium, Sc = 1 | 17.3 | 11.7 | 8.45 |
| Medium, Sc = 10 | 42.8 | 32.8 | 15.6 |
| Fine, Sc = 10 | 37.6 | 29.5 | 23.6 |

**Table 5**
Volume-averaged mean consumption rate (kmol/m$^3$s).

| | Nucleation | Growth |
|---|---|---|
| Medium, Sc = 1 | $1.692 \cdot 10^{-4}$ | 16.3763 |
| Medium, Sc = 10 | $1.752 \cdot 10^{-4}$ | 15.8275 |
| Fine, Sc = 10 | $1.673 \cdot 10^{-4}$ | 15.9995 |

the mixing channel after 0.5 mm. On the other hand, the first moment as computed from the higher Schmidt number simulation shows less crystal volume formed. Together, these findings may suggest that the consumption of reactants at elevated Schmidt number condition is slightly slower in general but also favours nucleation over growth due to the more confined high supersaturation zones. These behavioural changes in nucleation and growth at different Schmidt number may explain the small deviations in the PSD validation in Tang et al. (2020), where the predicted PSD (where $Sc = 1$ was employed) also featured a small underestimation of the peak of the PSD, while the shape of the distribution was slightly skewed on the larger end. However, uncertainties in kinetics and possibly experimental measurements, are likely to be of a higher order from the Schmidt number effects.

## 6. Conclusions

Conventional ways of modelling turbulent precipitation involve time-averaging or filtering the PBE and species transport equations. The turbulent fluctuations result in several unclosed terms that depict the effect of turbulent mixing. The present paper provided, for the first time, an analysis of these terms with the aid of a coupled DNS-PBE simulation of $BaSO_4$ precipitation in a T-mixer.

At first, the experiment of Schwarzer et al. (2006) with $Re = 1135$ on $BaSO_4$ precipitation in a T-mixer was simulated. As

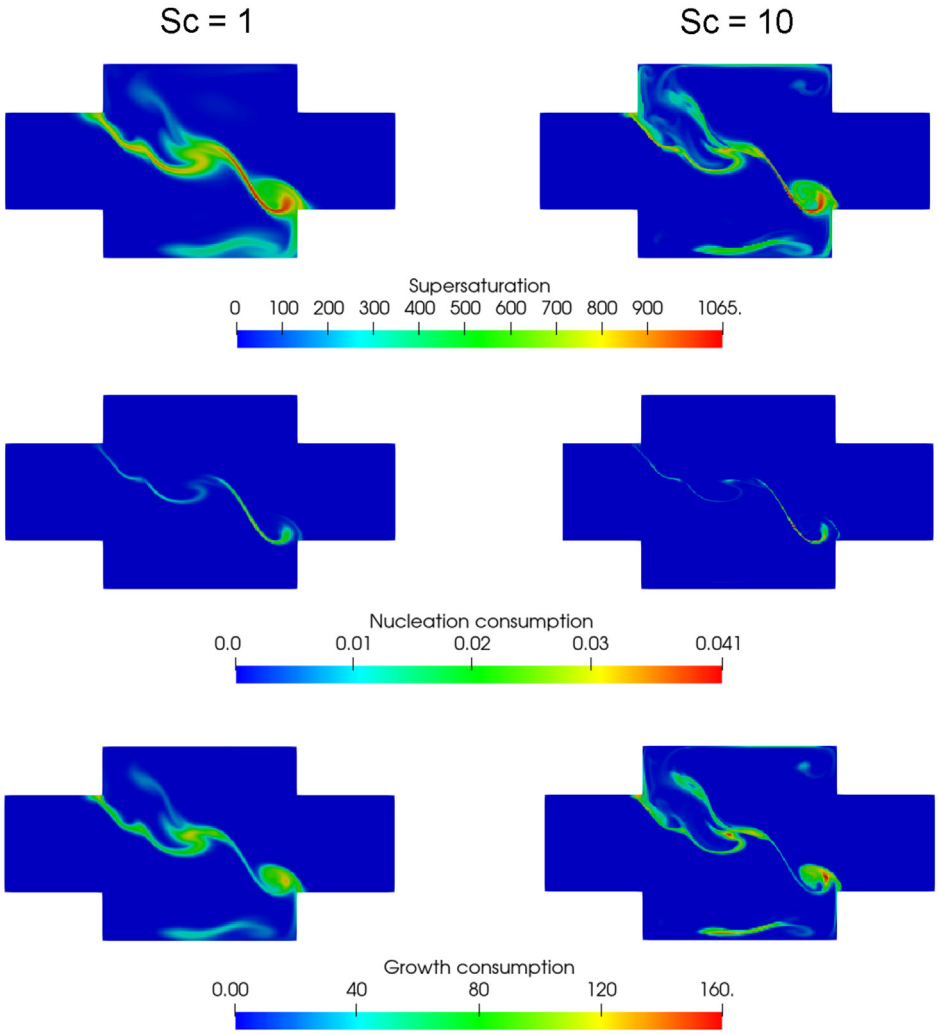


**Fig. 20.** Instantaneous supersaturation (top), nucleation consumption rate (middle) and growth consumption rate (bottom) contours at $Sc = 1$ (left) and $Sc = 10$ in the fine resolution (right).

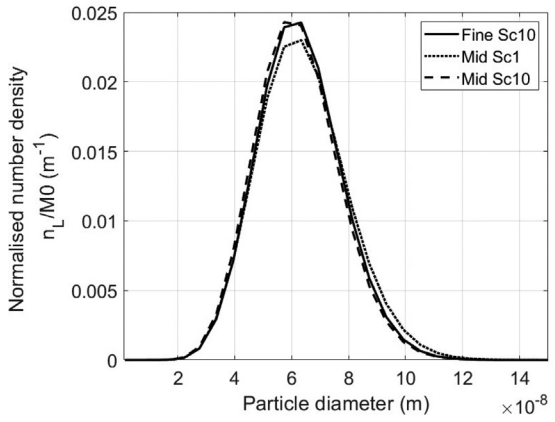


**Fig. 21.** Time- and plane-averaged particle size distribution.

it was not possible to resolve the sub-Kolmogorov scales at this geometry and Reynolds number, the simulation was performed with $Sc = 1$. The kinetic rates approximated with mean concentration were compared with the "true" mean rates (i.e. as evaluated by DNS-PBE) and significant differences were found, especially in intense precipitation regions. Subsequently, the number density-growth correlations were investigated. It was shown that negative correlations are found in areas of high mean growth rate since particle growth inherently relocates the number densities from lower intervals to higher intervals, causing number density reduction and hence negative correlation terms. On the other hand, nucleation generates particles and results in positive correlations at small size intervals. The gradient of these correlations in the particle size domain provides the fluctuation contribution in the PBE source term, whose magnitude was found to be significant for the PSD evolution. However, the effect of fluctuations on the reactant consumption term was found to be minimal, due to a compensation between positive and negative fluctuation terms.

The findings of the present study have implications for the modelling of precipitation. Neglecting or incorrectly modelling the PBE fluctuation terms, particularly the different sign of the fluctuation terms at small and large size intervals, could end up with a direct impact on the PSD shape, probably resulting in an underestimation of the total growth effect, causing the PSD shape to skew towards the lower end of the distribution. The modelling of these terms can be carried out by presumed or transported PDF methods, and examples of such works have been mentioned in Section 1. The transported PDF method is the most comprehensive approach, as it does not involve assumptions on the shape of the PDF, but it is also the most expensive, as it requires a stochastic method due to the

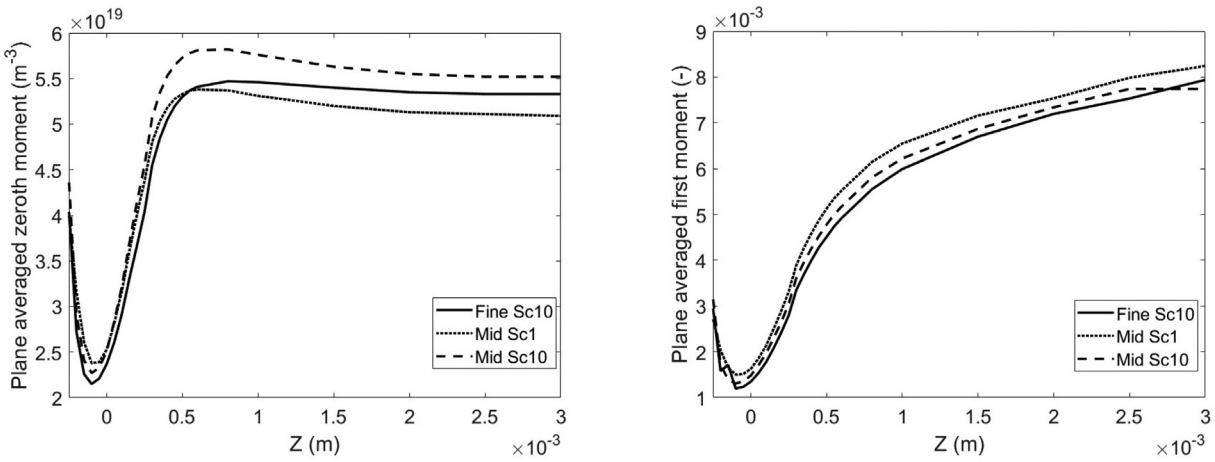


**Fig. 22.** Time- and plane-averaged zeroth moment (left) and first moment (right).

associated increase in dimensionality (dependent variables become independent ones in the PDF). In LES, the method of stochastic fields allows for implementing a transported PDF approach with as few as 8 fields (i.e. computing the scalar fields 8 times). Its implementation is straightforward and has been carried out for turbulent reacting flows with particles (the LES-PBE-PDF method, coupling discretised PBE and transported PDF) in the field of soot formation (Sewerin and Rigopoulos, 2018; Sun and Rigopoulos, 2022), so it may offer a direction for future work in turbulent precipitation as well.

The problem of high Schmidt number has been a well-known challenge in the modelling of mixing in liquid phase flow and is highly relevant to many chemical engineering applications. In the present study, an attempt was made to shed light into this problem by performing simulations of precipitation in a T-mixer at $Re = 400$ (the lowest possible value to achieve turbulent flow in a T-mixer) at $Sc = 1$ and $Sc = 10$. Comparisons of the reaction zone structures, magnitude of consumption rates and particle size distribution were made, in order to evaluate the influence of grid resolution, the effect of mixing at the sub-Kolmogorov scales and the impact of these scales on the kinetic rates and PSD. The results suggest that the effects of sub-Kolmogorov scales emerging at high *Sc* alter the process in several aspects. First, the reaction zones are more confined at high Schmidt number. Second, these thinner zones feature more intense precipitation rates. The extent of the reaction zones and intensity of the reaction rates to some extent compensate with each other, leading to similar average consumption and a marginal effect on the PSD. Third, there is a small difference between the consumption patterns of nucleation and growth; in the cases investigated here, the formation of nuclei is slightly more aggressive at low *Sc*, such that more particles may start growing at early stages. This eventually results in a PSD that is slightly biased on the larger end of the distribution and could be one of the causes of the minor discrepancies between simulations and measurements observed in Tang et al. (2020). However, uncertainties in other factors such as kinetics and possibly experiment measurements are likely to be of higher order.

Overall, the present study illuminated certain important issues related to the effect of turbulent fluctuations and micromixing on precipitation. The issue of high Schmidt number flows requires further study that may be possible to realise in future work.

## Declaration of Competing Interest

The authors declare that they have no known competing financial interests or personal relationships that could have appeared to influence the work reported in this paper.

## Acknowledgements

Hin Yan Tang gratefully acknowledges the financial support from the Department of Mechanical Engineering, Imperial College London in the form of a PhD studentship. Stelios Rigopoulos and George Papadakis gratefully acknowledge financial support from the Leverhulme Trust (grant RPG-2018–101). The authors are grateful to EPSRC (Grant No.: EP/R029369/1) and ARCHER for financial and computational support as a part of their funding to the UK Consortium on Turbulent Reacting Flows (www.ukctrf.com). We are also grateful to the UK Materials and Molecular Modelling Hub for computational resources on Thomas through EPSRC grant EP/P020194/1.

## References

Bałdyga, J., Bourne, J.R., 1984. A fluid mechanical approach to turbulent mixing and chemical reaction - Part II: Micromixing in the light of turbulence theory. Chem. Eng. Commun. 28 (4–6), 243–258.
Bałdyga, J., Bourne, J.R., 1984. A fluid mechanical approach to turbulent mixing and chemical reaction - Part III: Computational and experimental results for the new micromixing model. Chem. Eng. Commun. 28 (4–6), 259–281.
Bałdyga, J., Bourne, J.R., 1999. Turbulent Mixing and Chemical Reactions. John Wiley & Sons.
Bałdyga, J., Orciuch, W., 1997. Closure problem for precipitation. Chem. Eng. Res. Des. 75 (2), 160–170.
Bałdyga, J., Orciuch, W., 2001. Barium sulphate precipitation in a pipe - an experimental study and CFD modelling. Chem. Eng. Sci. 56 (7), 2435–2444.
Bałdyga, J., Podgórska, W., Pohorecki, R., 1995. Mixing-precipitation model with application to double feed semibatch precipitation. Chem. Eng. Sci. 50 (8), 1281–1300.
Bałdyga, J., Jasińska, M., Orciuch, W., 2003. Barium sulphate agglomeration in a pipe - an experimental study and CFD modeling. Chem. Eng. Technol. 26 (3), 334–340.
Bałdyga, J., Makowski, L., Orciuch, W., 2007. Double-feed semibatch precipitation: effects of mixing. Chem. Eng. Res. Des. 85 (A5), 745–752.
Başbuğ, S., Papadakis, G., Vassilicos, J.C., 2018. Reduced power consumption in stirred vessels by means of fractal impellers. AIChE J. 64 (4), 1485–1499.
Bromley, L.A., 1973. Thermodynamic properties of strong electrolytes in aqueous solutions. AIChE J. 19 (2), 313–320.
Buaria, D., Clay, M.P., Sreenivasan, K.R., Yeung, P.K., 2021. Small-scale isotropy and ramp-cliff structures in scalar turbulence. Phys. Rev. Lett. 126 (3), 034504.
David, R., 2001. General rules for prediction of the intensity of micromixing effects on precipitations. Powder Technol. 121 (1), 2–8.
David, R., Marcant, B., 1994. Prediction of micromixing effects in precipitation: case of double-jet precipitators. AIChE J. 40 (3), 424–432.
Davidson, P.A., 2004. Turbulence: An introduction for scientists and engineers. Oxford University Press.
Derksen, J.J., 2012. Direct simulations of mixing of liquids with density and viscosity differences. Ind. Eng. Chem. Res. 51 (19), 6948–6957.
Di Veroli, G., Rigopoulos, S., 2009. A study of turbulence-chemistry interaction in reactive precipitation via a population balance-transported PDF method. In: Hanjalić, K., Nagano, Y., Jakirlić, S. (Eds.), Turbulence, Heat and Mass Transfer 6. Proceedings of the Sixth International Symposium on Turbulence, Heat and Mass Transfer, Rome, Italy, Begell House, Inc., 2009.

Di Veroli, G., Rigopoulos, S., 2010. Modeling of turbulent precipitation: A transported population balance-PDF method. AIChE J. 56 (4), 878–892.
Donzis, D.A., Yeung, P.K., 2010. Resolution effects and scaling in numerical simulations of passive scalar mixing in turbulence. Physica D 239 (14), 1278–1287.
Donzis, D.A., Sreenivasan, K.R., Yeung, P.K., 2010. The Batchelor spectrum for mixing of passive scalars in isotropic turbulence: Submitted for the special issue dedicated to S.B. Pope. Flow, Turbul. Combust. 85 (3–4), 549–566.
Donzis, D.A., Aditya, K., Sreenivasan, K.R., Yeung, P.K., 2014. The turbulent Schmidt number. J. Fluids Eng. Trans. ASME 136 (6), 060912.
Falk, L., Schaer, E., 2001. A PDF modelling of precipitation reactors. Chem. Eng. Sci. 56 (7), 2445–2457.
Gavi, E., Marchisio, D.L., Barresi, A.A., 2007. CFD modelling and scale-up of Confined Impinging Jet Reactors. Chem. Eng. Sci. 62 (8), 2228–2241.
Gavi, E., Rivautella, L., Marchisio, D.L., Vanni, M., Barresi, A.A., Baldi, G., 2007. CFD modelling of nano-particle precipitation in confined impinging jet reactors. Chem. Eng. Res. Des. 85 (5 A), 735–744.
Gradl, J., Peukert, W., 2009. Simultaneous 3D observation of different kinetic subprocesses for precipitation in a T-mixer. Chem. Eng. Sci. 64 (4), 709–720.
Gradl, J., Schwarzer, H.-C., Schwertfirm, F., Manhart, M., Peukert, W., 2006. Precipitation of nanoparticles in a T-mixer: Coupling the particle population dynamics with hydrodynamics through direct numerical simulation. Chem. Eng. Process. 45 (10), 908–916.
Haworth, D., 2010. Progress in probability density function methods for turbulent reacting flows. Prog. Energy Combust. Sci. 36 (2), 168–259.
Jaworski, Z., Nienow, A.W., 2003. CFD modelling of continuous precipitation of barium sulphate in a stirred tank. Chem. Eng. J. 91 (2–3), 167–174.
Kucher, M., Babic, D., Kind, M., 2006. Precipitation of barium sulfate: Experimental investigation about the influence of supersaturation and free lattice ion ratio on particle formation. Chem. Eng. Process. 45 (10), 900–907.
Leer, M., Pettit, M.W.A., Lipkowicz, J.T., Domingo, P., Vervisch, L., Kempf, A.M., 2022. A conservative Eulerian-Lagrangian decomposition principle for the solution of multi-scale flow problems at high Schmidt or Prandtl numbers. J. Comput. Phys. 464, 111216.
Liu, A., Rigopoulos, S., 2019. A conservative method for numerical solution of the population balance equation, and application to soot formation. Combust. Flame 205, 506–521.
Liu, A., Garcia, C.E., Sewerin, F., Williams, B.A.O., Rigopoulos, S., 2020. Population balance modelling and laser diagnostic validation of soot particle evolution in laminar ethylene diffusion flames. Combust. Flame 221, 384–400.
Makowski, L., Orciuch, W., Bałdyga, J., 2012. Large eddy simulations of mixing effects on the course of precipitation process. Chem. Eng. Sci. 77, 85–94.
Marcant, B., David, R., 1991. Experimental evidence for and prediction of micromixing effects in precipitation. AIChE J. 37 (11), 1698–1710.
Marchisio, D.L., Fox, R.O., 2013. Computational Models for Polydisperse Particulate and Multiphase Systems. Cambridge University Press.
Marchisio, D.L., Barresi, A.A., Fox, R.O., 2001. Simulation of turbulent precipitation in a semi-batch Taylor-Couette reactor using CFD. AIChE J. 47 (3), 664–676.
Marchisio, D.L., Fox, R.O., Barresi, A.A., Garbero, M., Baldi, G., 2001. On the simulation of turbulent precipitation in a tubular reactor via computational fluid dynamics (CFD). Chem. Eng. Res. Des. 79 (8), 998–1004.
Marchisio, D.L., Fox, R.O., Barresi, A.A., Baldi, G., 2001. On the comparison between presumed and full PDF methods for turbulent precipitation. Ind. Eng. Chem. Res. 40 (23), 5132–5139.
Marchisio, D.L., Rivautella, L., Barresi, A.A., 2006. Design and scale-up of chemical reactors for nanoparticle precipitation. AIChE J. 52 (5), 1877–1887.
Mersmann, A. (Ed.), 2001. Crystallization Technology Handbook. 2nd Edition. Marcel Dekker.
Metzger, L., Kind, M., 2015. On the transient flow characteristics in Confined Impinging Jet Mixers - CFD simulation and experimental validation. Chem. Eng. Sci. 133, 91–105.
Metzger, L., Kind, M., 2017. The influence of mixing on fast precipitation processes – A coupled 3D CFD-PBE approach using the direct quadrature method of moments. DQMOM. Chem. Eng. Sci. 169, 284–298.
Monnin, C., 1999. A thermodynamic model for the solubility of barite and celestite in electrolyte solutions and seawater to 200°C and to 1 kbar. Chem. Geol. 153 (1–4), 187–209.
Öncül, A.A., Sundmacher, K., Seidel-Morgenstern, A., Thévenin, D., 2006. Numerical and analytical investigation of barium sulphate crystallization. Chem. Eng. Sci. 61 (2), 652–664.
O'Sullivan, D., Rigopoulos, S., 2022. A conservative finite volume method for the population balance equation with aggregation, fragmentation, nucleation and growth. Chem. Eng. Sci. 263, 117925.
Paul, I., Papadakis, G., Vassilicos, J.C., 2018. Direct numerical simulation of heat transfer from a cylinder immersed in the production and decay regions of grid-element turbulence. J. Fluid Mech. 847, 452–488.
Peters, N., 2000. Turbulent Combustion. Cambridge University Press.
Piton, D., Fox, R.O., Marcant, B., 2000. Simulation of fine particle formation by precipitation using computational fluid dynamics. Can. J. Chem. Eng. 78 (5), 983–993.
Pohorecki, R., Bałdyga, J., 1983. The use of a new model of micromixing for determination of crystal size in precipitation. Chem. Eng. Sci. 38 (1), 79–83.
Pohorecki, R., Bałdyga, J., 1988. The effects of micromixing and the manner of reactor feeding on precipitation in stirred tank reactors. Chem. Eng. Sci. 43 (8), 1949–1954.
Poinsot, T., Veynante, D., 2005. Theoretical and Numerical Combustion. Edwards.
Qamar, S., Elsner, M.P., Angelov, I.A., Warnecke, G., Seidel-Morgenstern, A., 2006. A comparative study of high resolution schemes for solving population balances in crystallization. Comput. Chem. Eng. 30 (6–7), 1119–1131.
Ranjan, R., Menon, S., 2021. Two level simulation of Schmidt number effect on passive scalar transport in wall-bounded turbulent flows. Phys. Fluids 33 (3), 035124.
Rigopoulos, S., 2007. PDF method for population balance in turbulent reactive flow. Chem. Eng. Sci. 62 (23), 6865–6878.
Rigopoulos, S., 2010. Population balance modelling of polydispersed particles in reactive flows. Prog. Energy Combust. Sci. 36 (4), 412–443.
Rigopoulos, S., Jones, A., 2003. A hybrid CFD-reaction engineering framework for multiphase reactor modelling: basic concept and application to bubble column reactors. Chem. Eng. Sci. 58 (14), 3077–3089.
Schwarzer, H.-C., Peukert, W., 2002. Experimental investigation into the influence of mixing on nanoparticle precipitation. Chem. Eng. Technol. 25 (6), 657–661.
Schwarzer, H.-C., Peukert, W., 2004a. Combined experimental/numerical study on the precipitation of nanoparticles. AIChE J. 50 (12), 3234–3247.
Schwarzer, H.-C., Peukert, W., 2004b. Tailoring particle size through nanoparticle precipitation. Chem. Eng. Commun. 191 (4), 580–606.
Schwarzer, H.-C., Peukert, W., 2005. Prediction of aggregation kinetics based on surface properties of nanoparticles. Chem. Eng. Sci. 60 (1), 11–25.
Schwarzer, H.-C., Schwertfirm, F., Manhart, M., Schmid, H.-J., Peukert, W., 2006. Predictive simulation of nanoparticle precipitation based on the population balance equation. Chem. Eng. Sci. 61 (1), 167–181.
Schwertfirm, F., Gradl, J., Schwarzer, H.C., Peukert, W., Manhart, M., 2007. The low Reynolds number turbulent flow and mixing in a confined impinging jet reactor. Int. J. Heat Fluid Flow 28 (6), 1429–1442.
Seckler, M.M., Bruinsma, O.S.L., Van Rosmalen, G.M., 1995. Influence of hydrodynamics on precipitation: A computational study. Chem. Eng. Commun. 135 (1), 113–131.
Sewerin, F., Rigopoulos, S., 2017. An explicit adaptive grid approach for the numerical solution of the population balance equation. Chem. Eng. Sci. 168, 250–270.
Sewerin, F., Rigopoulos, S., 2018. An LES-PBE-PDF approach for predicting the soot particle size distribution in turbulent flames. Combust. Flame 189, 62–76.
Sun, B., Rigopoulos, S., 2022. Modelling of soot formation and aggregation in turbulent flows with the LES-PBE-PDF approach and a conservative sectional method. Combust. Flame 242, 112152.
Sun, B., Rigopoulos, S., Liu, A., 2021. Modelling of soot coalescence and aggregation with a two-population balance equation model and a conservative finite volume method. Combust. Flame 229, 111382.
Tang, H.Y., Rigopoulos, S., Papadakis, G., 2020. A methodology for coupling DNS and discretised population balance for modelling turbulent precipitation. Int. J. Heat Fluid Flow 86, 108689.
Tang, H.Y., Rigopoulos, S., Papadakis, G., 2022. On the interaction of turbulence with nucleation and growth in reaction crystallisation. J. Fluid Mech. 944, A48.
Tavare, N.S., 1986. Mixing in continuous crystallizers. AIChE J. 32 (5), 705–732.
Telib, H., Manhart, M., Iollo, A., 2004. Analysis and low-order modeling of the inhomogeneous transitional flow inside a T-mixer. Phys. Fluids 16 (8), 2717–2731.
Thomareis, N., Papadakis, G., 2017. Effect of trailing edge shape on the separated flow characteristics around an airfoil at low Reynolds number: A numerical study. Phys. Fluids 29 (1), 014101.
Thomareis, N., Papadakis, G., 2018. Resolvent analysis of separated and attached flows around an airfoil at transitional Reynolds number. Phys. Rev. Fluids 3, 073901.
Tsagkaridis, M., Rigopoulos, S., Papadakis, G., 2022. Analysis of turbulent coagulation in a jet with discretised population balance and DNS. J. Fluid Mech. 937, A25.
Van Leeuwen, M.L.J., Bruinsma, O.S.L., Van Rosmalen, G.M., 1996. Influence of mixing on the product quality in precipitation. Chem. Eng. Sci. 51 (11), 2595–2600.
Vicum, L., Mazzotti, M., 2007. Multi-scale modeling of a mixing-precipitation process in a semibatch stirred tank. Chem. Eng. Sci. 62 (13), 3513–3527.
Vicum, L., Mazzotti, M., Bałdyga, J., 2003. Applying a thermodynamic model to the non-stoichiometric precipitation of barium sulfate. Chem. Eng. Technol. 26 (3), 325–333.
Villermaux, J., 1989. A simple model for partial segregation in a semibatch reactor. In: AIChE Meeting San Francisco, Paper 114a.
Wei, H., Garside, J., 1997. Application of CFD modelling to precipitation systems. Chem. Eng. Res. Des. 75 (2), 219–227.
Wei, H., Zhou, W., Garside, J., 2001. Computational fluid dynamics modeling of the precipitation process in a semibatch crystallizer. Ind. Eng. Chem. Res. 40 (23), 5255–5261.
Woo, X.Y., Tan, R.B.H., Chow, P.S., Braatz, R.D., 2006. Simulation of mixing effects in antisolvent crystallization using a coupled CFD-PDF-PBE approach. Cryst. Growth Des. 6 (6), 1291–1303.
Xiao, D., Papadakis, G., 2017. Nonlinear optimal control of bypass transition in a boundary layer flow. Phys. Fluids 29 (5), 054103.
Xiao, D., Papadakis, G., 2019. Nonlinear optimal control of transition due to a pair of vortical perturbations using a receding horizon approach. J. Fluid Mech. 861, 524–555.
Zauner, R., Jones, A.G., 2000. Scale-up of continuous and semibatch precipitation processes. Ind. Eng. Chem. Res. 39 (7), 2392–2403.